

Depositional and diagenetic processes in volcanic matrix-rich sandstones from the Shanxi and Shihezi formations, Ordos Basin, China: Implication for volcano-sedimentary systems

CUI ET AL. **Hang Cui**^{1,2} | **Shifa Zhu**^{1,2} | **Mingxuan Tan**³ | **Huan Tong**^{1,2}

¹State Key Laboratory of Petroleum Resources and Prospecting, China University of Petroleum (Beijing), Beijing, China

²College of Geosciences, China University of Petroleum, Beijing, China

³College of Oceanography, Hohai University, Nanjing, China

Correspondence

Shifa Zhu, State Key Laboratory of Petroleum Resources and Prospecting, China University of Petroleum (Beijing), Beijing 102249, China.
Email: sfzhu@cup.edu.cn

Funding information

National Natural Science Foundation of China, Grant/Award Number: 41202107 and 41872102

Abstract

Volcanic eruptions can provide large amounts of sedimentary materials and expose fluvial valleys or lakes to catastrophic hyperpycnal flood events, but this process has not been documented in detail. The Ordos Basin Permian fluvio-deltaic system reveals evidence for abundant volcanism linked to the tectonic evolution of orogenic belt around the basin and provides a ‘natural laboratory’ for investigating hyperpycnal flows associated with volcanic activity. This study analysed volcanic matrix-rich sandstone (VMS) samples for petrology, mineralogy and geochemistry in order to address current and uncertain volcanogenic material provenance explanations and the lack of systematic investigations into the depositional and diagenetic processes of volcanic related sediments in the southwestern basin. By combining tectonic background surveys, detrital zircon geochronology and spatial distribution of volcanogenic materials, it was found that volcanogenic materials were not derived from the Yinshan-Yanshan Orogenic Belt (YYOB) as previously thought, but instead evidence a southwestern origin from the North Qinling Orogenic Belt (NQOB). Volcanogenic materials retained in the provenance area during frequent volcanic eruptions were transported to the basin via fluvial systems shortly after the eruption. The associated sediments meet the criterion for hyperpycnites based on lithofacies associations, suggesting the occurrence of hyperpycnal flows during the deposition of VMS. During the subsequent burial stage, the VMS became three distinct types defined by their volcanic matrix content and have similar paragenetic sequences but different diagenetic intensities. The differing content of authigenic minerals in the three types was closely related to the sandstone pore structure characteristics and the evolution of volcanic-matrix alteration materials. This article proposes a possible explanation for the previously unidentified tectonothermal events in the NQOB during the Permian, validating and reinforcing the theoretical work of hyperpycnal flow. This contribution provides new insights and understanding of the depositional and diagenetic processes of lacustrine basins with similar tectonic settings.

KEYWORDS

hyperpycnal flow, Ordos Basin, paragenetic sequence, provenance area, volcanic matrix-rich sandstone, volcanogenic materials

1 | INTRODUCTION

Complex interrelationships may exist between topography, depositional systems and volcanism in volcanically active basins (Chen et al., 2022; Lenhardt et al., 2011; Magee et al., 2014). Previous studies suggest that voluminous volcanic eruptions are likely to change surface topography, increase the occurrence of landslides, locally block or create axial fluvial systems, modify existing sedimentary settings and even re-establish fluvial, lacustrine and marine environments (e.g., Ebinghaus et al., 2014; Magee et al., 2013; Reidel & Tolan, 2013). Additionally, explosive volcanism can greatly enhance the density of river discharges and provide large amounts of volcanogenic materials to resulting sedimentary deposits (Mulder et al., 2001, 2003; Plink-Björklund & Steel, 2004). These volcanogenic materials generated by paroxysmal volcanic eruptions can propagate over considerable distances through air, water or a combination thereof (White & Houghton, 2006). For subaerial eruptions, the extent and thickness of volcanogenic materials are influenced by syn-depositional factors (including eruption volume, proximity to volcanic centres, pre-volcanic paleo-topography, prevailing wind direction) and post-depositional processes (including reworking or mixing due to waves, storms, sediment dilution and condensation) (Hong et al., 2019; Millett et al., 2021; Ver Straeten, 2004). The sedimentary sequences associated with volcanism provide an abundance of evidence about the volcanic history linked to tectonic evolution and depositional processes (Richards et al., 2005). However, it is still challenging to make an accurate assessment of the sedimentary processes and tectonic significance of volcanogenic materials based on their petrological and geochemical characteristics.

There is increasing evidence of a direct and abundant supply of sediment from rivers in flood to the inner basin via hyperpycnal flows (Zavala & Arcuri, 2016), providing new perspectives for the understanding of fluvio-deltaic system. Frequent tectonic movements and earthquakes, large topographic slope, seasonal floods and typhoons are the main controlling factors for triggering hyperpycnal flow (e.g., Mulder & Syvitski, 1995; Mutti et al., 2003; Plink-Björklund & Steel, 2004; Zavala et al., 2006). Compared with marine environments, lacustrine basins are more sensitive to sediment dispersal processes, making them easier to cause hyperpycnal flow (Liu et al., 2021). In tectonically active mountain belts, explosive volcanic eruptions favour the breaking of

Highlights

- Petrology, mineralogy and geochemistry from the Ordos Basin provide insight into volcano-sedimentary systems.
- Multi-volcanic-material source existed during the Permian of the Ordos Basin.
- Sedimentary analysis validates and reinforces the theoretical work of hyperpycnal flow.
- Intensive element migration can occur during the burial alteration of volcanic matrix.

temporary dam lakes, exposing fluvial valleys and lakes to catastrophic hyperpycnal flood events (Dadson et al., 2004; Mulder et al., 2003). Due to the long periodicity and unpredictability of volcanic events, there has not been an applicable case for linking hyperpycnal flows with volcanic activity in any modern fluvio-deltaic system. However, the ancient Permian fluvio-deltaic system in the Ordos Basin provides a 'natural laboratory' for researching the link between hyperpycnal flow processes and volcanic activity.

Due to their poor chemical stability, volcanogenic materials are more likely to be devitrified or altered during the process of reservoir diagenesis (Summa & Verosub, 1992). In particular, microcrystalline and highly reactive volcanic ash with a large surface area can exert a stronger influence on diagenetic processes than volcanic debris (Hesse & Schacht, 2011; Murray et al., 2018). Alteration of volcanogenic materials contributes to precipitation of different authigenic minerals and (re)crystallisation of various mineral phases (e.g., clay minerals, zeolites, calcite and dolomite) (Antibus et al., 2014; Capo et al., 2000; Dill, 2016; Fisher & Schmincke, 1984; Huff, 2016; Spears, 2012; Zhu et al., 2019). Therefore, the prediction and evaluation of volcanogenic material alteration play an important role in the reservoir diagenesis of deeply buried prospects. Although the alteration processes of volcanic ash and its resulting products have been extensively studied (Crovisier et al., 1983), previous work mainly focused on individual volcanic ash beds, with only a few studies investigating diagenetic characteristics, chemical reaction and material transformation between terrestrial debris and volcanic ash matrix.

The volume fraction of volcanogenic materials was generally between 5.0% and 17.0% in the Upper Palaeozoic sandstone reservoirs of the Ordos Basin (Yang et al., 2006).

These volcanogenic materials were determined to be derived from volcanism at the orogenic belt of the Ordos Basin margin (Shen et al., 2017). However, questions still remain: Were the volcanogenic materials in different regions of the same provenance attribute? How can volcanic ash be deposited in large quantities mixed with terrigenous debris via long-distance transport? How did these volcanogenic materials affect reservoir quality during the diagenesis? Therefore, the purpose of this study is to: (1) present new conjecture on the origin of volcanogenic materials and reveal the possible tectonothermal events in the southwest margin of the basin during the Permian; (2) confirm the existence of hyperpycnal flows in fluvio-deltaic system and establish a link between volcanism and hyperpycnal flows and (3) examine the diagenetic processes involved in volcanic matrix alteration.

2 | GEOLOGIC SETTING

The Ordos basin is a typical multi-cycle superposed petroliferous basin in China (Zhu et al., 2020). It can be divided into six first-order tectonic units based on their structural evolution (He et al., 2017; Tan et al., 2019). The study area, the Longdong Region, is located in the southwestern part of Ordos Basin southwest of the Yishaan Slope and southeast of the Tianhuan Depression, covering approximately 54,000 km² (Figure 1a).

The Yinshan-Yanshan Orogenic Belt (YYOB) in the north and the Qinling Orogenic Belt (QOB) in the south became two major provenance areas during the Late Palaeozoic (Figure 1a,d) (Chen et al., 2021; Liang et al., 2020). The northern boundary was the active continental margin in the Permian, and the subsequent collision between the Siberian plate and the North China plate resulted in the extinction of the Paleo-Asian Oceanic Crust and the relative uplift of the northern YYOB (Zhang et al., 2007; Zhao et al., 2016). The QOB is a composite continental orogenic belt with complex crustal composition and structure, which can be further divided into two parts: The South Qinling Orogenic Belt (SQOB); and the North Qinling Orogenic Belt (NQOB) (Dong et al., 2011). During the Late Palaeozoic, the Mianlue Oceanic Crust gradually subducted to the north, with a transform tendency from passive to active continental margin (Figure 1d) (Ratschbacher et al., 2003). The NQOB uplift occurred earlier, and it is believed that the northern margin of the Shangdan Ocean crust began to subduct northward under the North China Craton (i.e., the Ordos Basin) around 530–470 Ma (Dong & Santosh, 2016). After the closure at ca. 450 Ma, the collision between the NQOB and the North China Craton (the Ordos Basin) occurred, followed by rapid uplift accompanied by tectonothermal events (Figure 1d) (Dong et al., 2011).

The basin's floor is composed of Archean and Lower Proterozoic metamorphic rocks, and the sedimentary cover is composed of Lower Palaeozoic marine carbonate rocks, Upper Palaeozoic littoral clastic rocks and Mesozoic continental clastic rocks (Zhu et al., 2017). During the Caledonian orogeny, the basin was gradually uplifted becoming denuded by the Middle Ordovician, resulting in the erosion or sedimentary hiatus of the Upper Ordovician, Silurian, Devonian and Lower Carboniferous strata. The Carboniferous-Permian coal-measure petroleum system, which developed during the craton depression stage of the basin, includes the Carboniferous Benxi Formation (C_3b), the Lower Permian Taiyuan Formation (P_1t) and Shanxi Formation (P_2s), the Middle Permian Lower Shihezi Formation and Upper Shihezi Formation (P_2h), and Shiqianfeng Formation (P_3q) of the Upper Permian (Figure 2) (Chen et al., 2021). The Shanxi 1 Member (P_2s_1) of P_2s and Shihezi 8 Member (P_2h_8) of P_2h was the main study interval. Tuffaceous sandstones are widely distributed at the bottom of these two members. Meandering-river deltas were developed during the sedimentary period of P_2s_1 (Figure 1b) (Zhu et al., 2021). However, due to gradual climate change from humid to arid, the delta plain area expanded in the sedimentary period of P_2h_8 and the sedimentary facies gradually changed into braided river-delta systems (Figure 1c) (Zhu et al., 2021).

3 | SAMPLES AND ANALYTICAL TECHNIQUES

In this study, 794.5 m of cores extracted from 32 wells of P_2h_8 and P_2s_1 in the Longdong Region were examined. Depositional processes identified in cores were described in detail, including lithology, grain-size variations, support mechanism, sedimentary structures, plant/mica remains and colour. Analyses of flow types and processes were performed through lithofacies classification and interpretation, followed by the determination of sedimentary environments. To observe and discuss the diagenesis involving volcanogenic materials, more than 300 samples from 32 cored wells were collected for various petrographic and geochemical analyses. These selected samples were mostly from medium-grained sandstones to fine-grained conglomerates (average grain size ranges from 0.25 to 10 mm) because the diagenetic phenomena of these deposits are more prominent than that observed in other lithologies.

3.1 | Petrography and scanning electron microscopy

A total of 276 thin sections were made to investigate mineralogical characteristics, occurrences and habits.

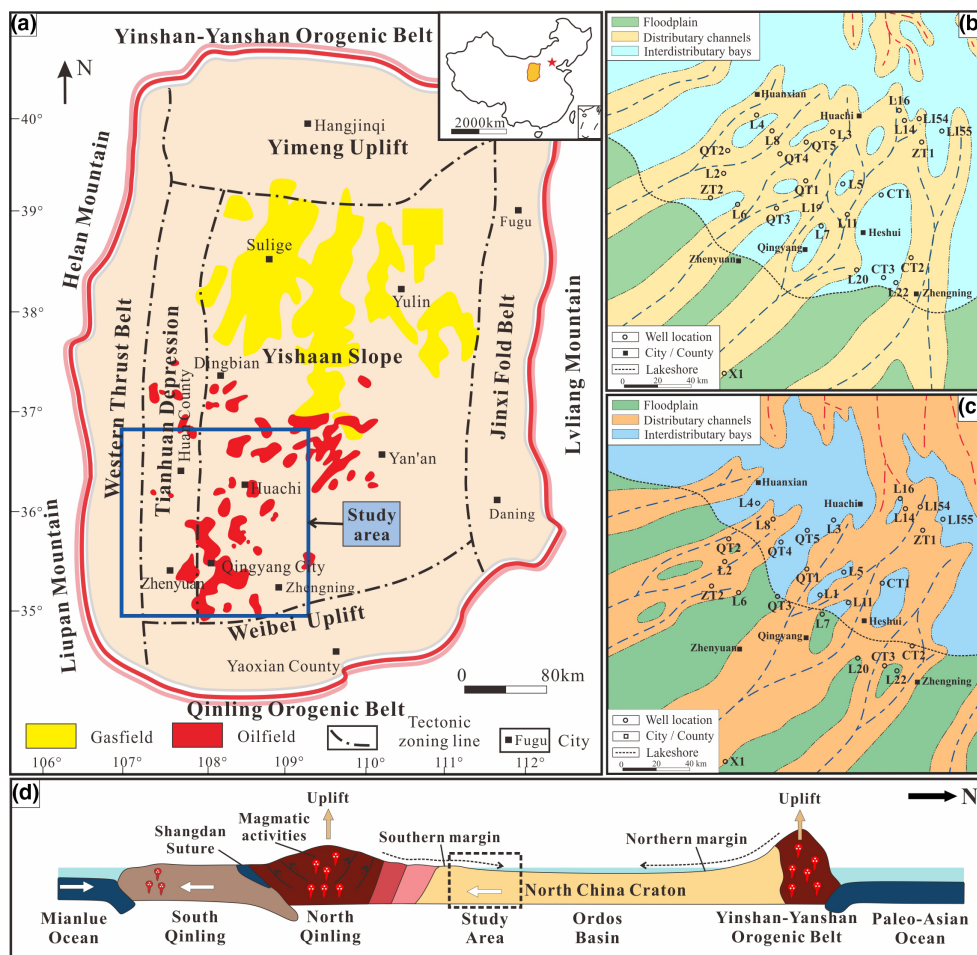


FIGURE 1 (a) Main geotectonic units of the Ordos Basin and location of the study area (modified from Zhu et al., 2020); (b) Distribution of the sedimentary facies of P_2S_1 ; (c) Distribution of the sedimentary facies of P_2h_8 ; (d) Regional tectonic model of the Ordos Basin and north–south orogenic belt during the Permian (modified from Dong et al., 2011; Dong & Santosh, 2016; Jiang et al., 2020).

More than half were impregnated with blue epoxy resin to observe pore characteristics, and some were stained with alizarin red-S solution. All the images were captured by metallographic microscope BX51 produced by Olympus, and the optical acquisition system is Olympus Stream provided by Olympus Soft Imaging Solutions GmbH. Images were photographed under the same conditions at a resolution of 2400×1800 pixels and stored as a JPG file.

Grain size measurements were performed with an automatic image-analysis microscope in a stable environment, with a temperature of 25°C and a humidity of 60%. Thin section grain size images required more than 400 grains per sample. The computer automatically summarised grain size distribution based on predefined parameters and drew cumulative curves. The curve shape reflects conditions of the sediment transport process and thus can be used as a tool in environmental interpretation (Boggs, 2006).

CL8200 Mk-2 model system of Cambridge Image Technology Ltd was used for Cathodoluminescence (CL),

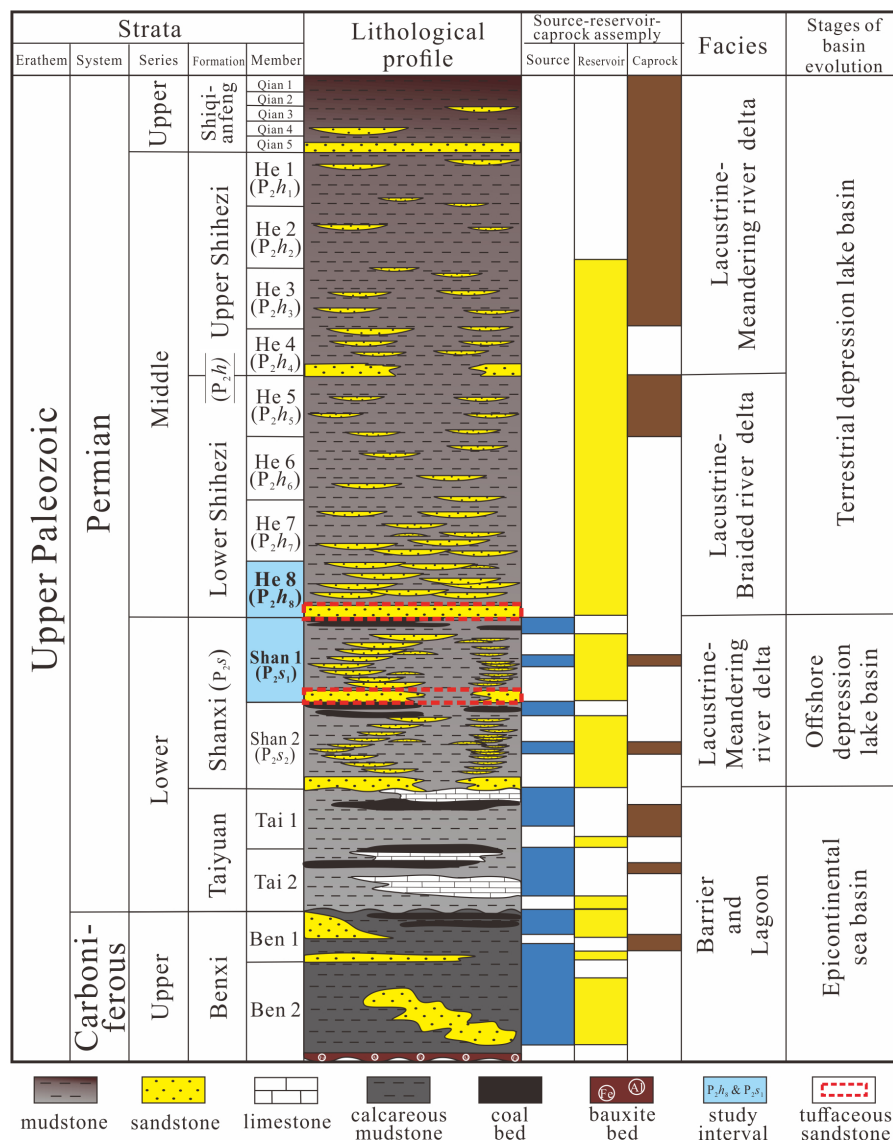
attached to a microscope with a camera system. The stable electron beam can reach a voltage of 10–30 kV and a current value of 100–300 mA. Because the samples differed in luminescence, the exposure time varied from 1 to 8 s was taken to ensure the image clarity.

Seven VMS samples were selected for surface and morphology observation. SEM-Hitachi-SU8010 and energy dispersive spectroscopy (EDS) attached to scanning electron microscopy were adopted for this analysis. To capture better images, a gold film was coated onto the surface of freshly broken rock. At high acceleration voltage (20 kV), the SU8100's secondary electron image resolution is 1 nm. The accelerated voltage ranges from 0.1 to 30 kV, and the magnification ranges from $\times 20$ to $\times 800,000$.

3.2 | Geochemistry

A quantitative analysis of major elemental compositions was conducted, and backscattered electron (BSE) images

FIGURE 2 Simplified stratigraphic column for the Carboniferous and Permian in the Ordos Basin. The VMS were mainly distributed at the bottom of P_2s_1 and P_2h_8 .



were obtained for six samples with a JEOL JXA-8100 electron microprobe. We focused on in-situ elemental composition of altered volcanic ash and its associated clay minerals in these samples. Experimental conditions were set as follows: voltage is 15 kV; current is 10 nA and electron beam diameter is 1 μ m. Magnification ranges from $\times 30$ to $\times 40,000$ and the analytical range is element atomic with numbers 5 to 92 (B–U).

The content of trace and rare earth elements in six tuff samples that lacked terrigenous detrital grains were measured in this study. The grain size of the samples was ground to 74 μ m or less and analysed via the sensitive quadrupole-based ICP-MS (ICP-QMS, XSeries2, Thermo Fisher Scientific, Bremen, Germany). The samples were pre-dried at 105°C for 2–4 h and cooled down to room temperature in the drying oven. Then the samples were dissolved by HNO_3 (42 g/ml) and HF (16 g/ml) in a closed reaction vessel. The hydrofluoric acid was evaporated on a hot plate after complete reaction. Finally, a further 25 ml

of HNO_3 and water were added for the determination of ICP-MS. The analytical precision for all elements is <5% based on the duplicate analyses of samples and standards (National Standards in China, DZ/T0223-2001).

3.3 | Fluid inclusions

Five silicone-cement-rich samples were selected for fluid inclusion homogenisation temperature and ice-melting temperatures. This experiment was performed on the Linkam THMS-600 heating and freezing stage (Temperature: 26°C, Humidity: 35%, Temperature measurement range: –100 to 400°C). Prior to conducting measurements, petrographic observations were required to characterise the size, shape, occurrence of fluid inclusions and the proportion of liquid versus gas phases. The measurements of homogenisation temperature preceded the freezing runs to avoid stretching of the inclusions by

ice nucleation. During heating runs, the heating rate was 10°C/min decreasing to 1–2°C/min when approaching the to the phase transition point. During cooling runs, the fluid inclusions were frozen completely and then the temperature was increased at a heating rate of no more than 0.5°C/min. The salinity was calculated by measuring the melting point temperature following ice points of H₂O–NaCl (Bodnar, 1993).

4 | FACIES ANALYSES

According to the colour, sedimentary structure and grain size characteristics, 13 lithofacies (LF) are recognised. Detailed descriptions of different lithofacies are shown in Figures 3 and 4. Based on the occurrence of different lithofacies, five principal facies associations (FA) (Figure 4) in the P₂S₁ and P₂h₈ are identified and delineated.

4.1 | Facies association 1

4.1.1 | Description

FA1 corresponds mainly to conglomerates and sandstones deposits arranged into a series of fining-upward cycles. The deposits are typically 1–1.5 m in thickness and as single layers. Greyish-white structureless conglomerates (LF1, Figure 4a) and normally graded conglomerates (LF2, Figure 4b) (thickness <30 cm) are observed at the bottom of the single sand bodies with low sorting and a common matrix-supported texture. Towards the middle of the single sand bodies, the deposits are constituted by planar-bedded or low-angle-stratification fine-grained conglomerates (LF3, Figure 4c). The gravels are mainly imbricated following diffuse subhorizontal alignments. Additionally, fine-grained conglomerates interbedded with pebbly sandstones with diffuse lamination (LF4, Figure 4d) are also developed and sometimes indistinguishable from LF3. The thicknesses of LF3 and LF4 can reach tens of centimetres but generally cannot exceed 60 cm. These two lithofacies are dominated by clast-supported textures, although matrix-supported textures do exist. Compared with LF1 to LF2, the sorting varies from moderate to good. The top of single sand bodies is characterised by planar-bedded pebbly sandstones (LF5, Figure 4e) and trough or tabular cross-bedded pebbly sandstones (LF6) ranging from 0.4 to 1 m thick.

4.1.2 | Interpretation

Structureless conglomerates (LF1) and normally graded conglomerates (LF2) are common as channel-filling gravel

sheets, which are often identified as erosional surfaces related to channel migration (Ebinghaus et al., 2014). These deposits are attributed to rapid deposition as a result of floods or levee breaches (Collinson, 1996). According to the conceptual schema associated with hyperpycnal systems proposed by Zavala et al. (2011), LF1 and LF2 can be regarded as Facies B1 (bedload, massive and crudely stratified conglomerates with abundant matrix), which are interpreted as gravel-rich traction current. Planar-bedded or low-angle-stratification fine-grained conglomerates (interbedded with pebbly sandstones) (LF3 and LF4) may also occur after floods or high flow stages (Ebinghaus et al., 2014). Irregular interbedding of fine-grained conglomerates with pebbly sandstones may be associated with periods of increasing or decreasing discharge during floods (Mulder et al., 2001, 2003). At the top of the single sand bodies, planar-bedded pebbly sandstones (LF5) and trough or tabular cross-bedded pebbly sandstones (LF6) are the results of migrating dunes in fluvial channels (Ebinghaus et al., 2014). LF5 and LF6 are attributed to Facies B3 (pebbly sandstones with diffuse subhorizontal stratification) and Facies B2 (pebbly sandstones with low-angle asymptotic cross-stratification), respectively (Zavala et al., 2011). Accordingly, these deposits are interpreted by the combined effect of bed load and the gravitational segregation of sandstone materials transported in the overpassing hyperpycnal turbulent flow (Zavala et al., 2011).

Therefore, this FA is identified as having been deposited in multi-phase conglomeratic-sandy distributary channels dominated by flood events (Miall, 1985; Xian et al., 2018).

4.2 | Facies association 2

4.2.1 | Description

FA2 is comprised principally of brick-red, greenish grey, light grey and variegated mudstones and siltstones, which may be interbedded with thin layers of fine-grained sandstones. The mudstones and siltstones are observed with planar lamination, wavy bedding (LF12) or structurelessness containing fossil flora remains (LF13), while the interbedded fine-grained sandstones generally display weak traction structure (such as wedge cross stratification and low-angle cross stratification) with individual lamination and a thickness of less than 0.5 cm. These deposits are common in the study area, varying in thickness from tens of centimetres to a few metres for a single unit.

4.2.2 | Interpretation

The brick-red colour suggests oxidising conditions, while the occurrence of discontinuous silt levels reflects alternating high

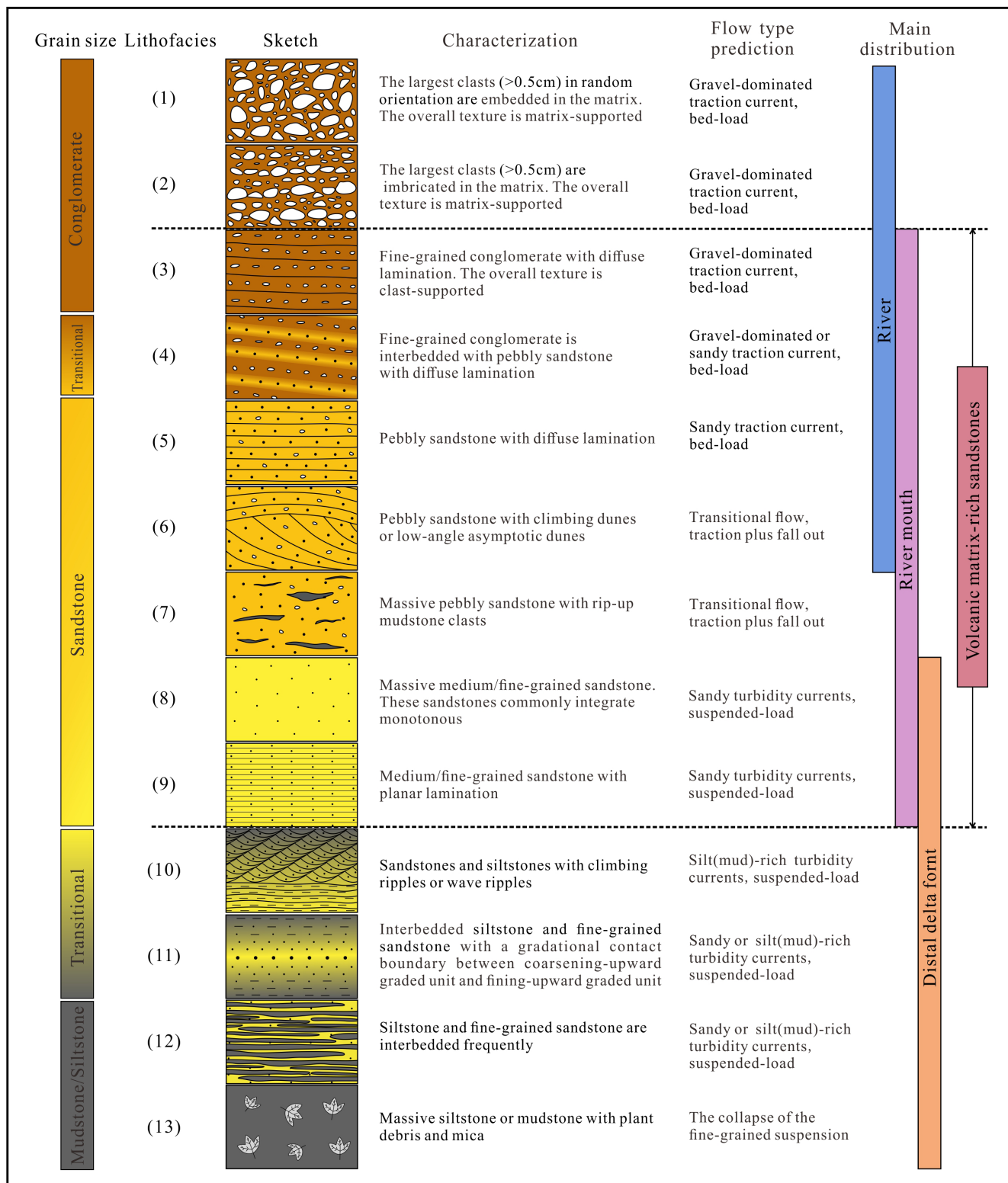
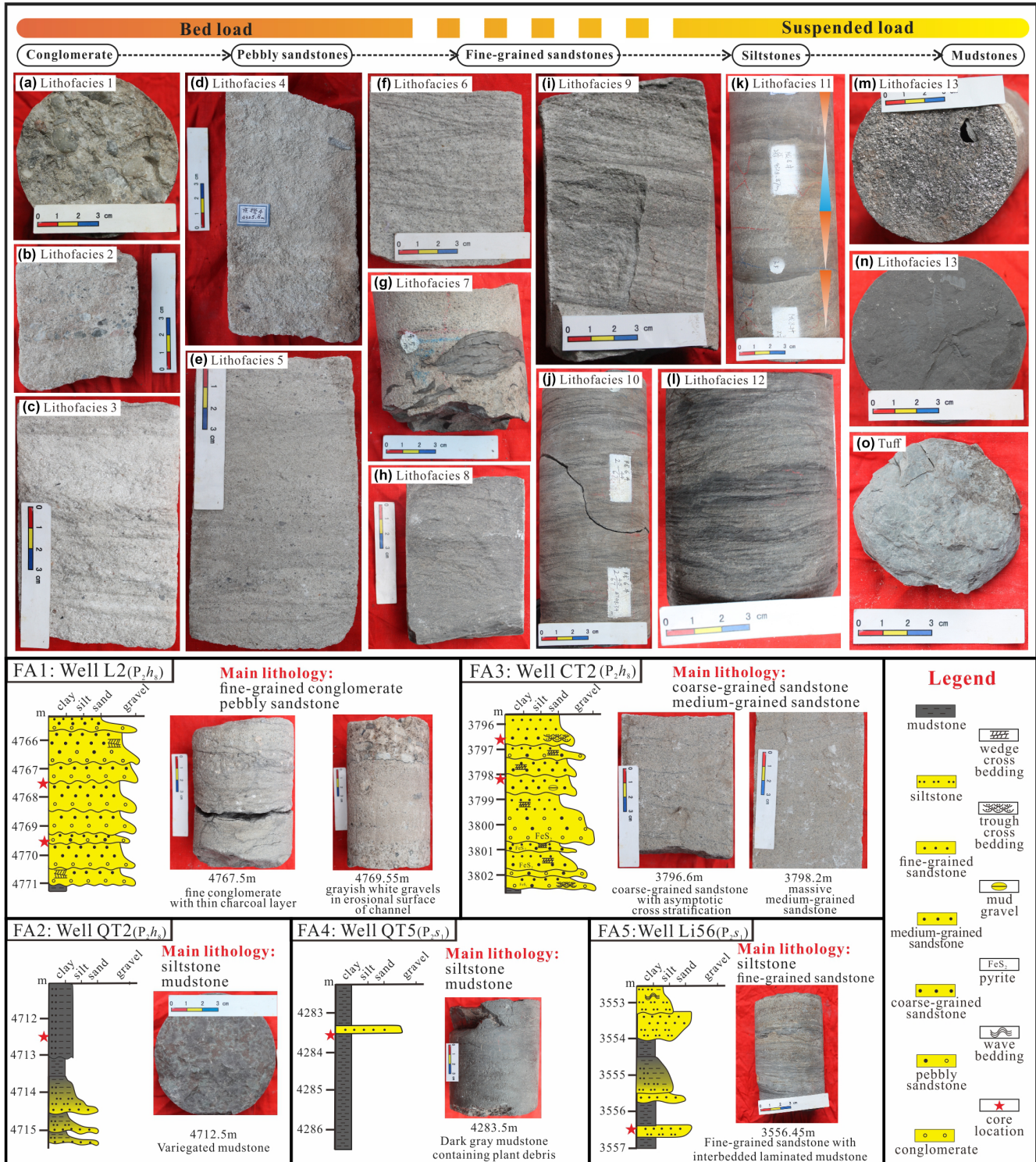


FIGURE 3 Conceptual schema and characteristics of 13 lithofacies recognised in the study area. Lithofacies are divided mainly by grain size and sedimentary structures. From Lithofacies 1 to Lithofacies 13, there may be a transformation from traction to turbidity current. VMS are mostly distributed in Lithofacies 3 to Lithofacies 9.

and low river energy and discharge (Liu et al., 2022). Therefore, silt deposition may take place after floods and during an increased flow stage (Ebinghaus et al., 2014), and the mud

deposition may have formed during a decreasing flow stage. Accordingly, FA2 is interpreted here as the settling of silt and mud suspension in a fluvial overbank (Paredes et al., 2009).



4.3 | Facies association 3

4.3.1 | Description

Mainly composed of clast-supported sandstones, the FA3 deposits are typically 0.2–1.0 m in thickness and as single layers. This FA shows a fining upwards tendency. Fine-grained conglomerates interbedded with pebbly sandstone (LF4, Figure 4d) are observed at the 10 to 30 cm

thick basal portion of the unit. Internally, the fine-grained conglomerates are imbricated and are seen to follow diffuse subhorizontal alignments. Pebbly sandstones with traction structures (e.g., wedge cross stratification, low-angle cross stratification and diffused lamination) (LF5 and LF6, Figure 4f) are observed above LF4. Light grey-coloured pebbly sandstones with floating clasts (LF7, Figure 4g) are occasionally observed jointly with LF5 and LF6. These floating clasts are generally dark-coloured

rip-up mud, reaching 8 cm in length and commonly exhibited horizontal alignment. The middle and top of the single sand bodies gradually changes into fine-grained sandstone with massive and parallel stratification (LF8, Figure 4h and LF9, Figure 4i). Commonly integrated monotonously and homogeneously, internally these two lithofacies show subtle and gradual grain-size variations.

Although FA3 evidenced remarkably similar characteristics to FA1, it differs in the lower proportion of conglomerates and the monotonous and homogeneous fine/medium-grained sandstones at the top of the units.

4.3.2 | Interpretation

Compared with FA1, the decrease in gravel concentration and flow momentum is more obvious in FA3. The single sand bodies can be vertically divided into two parts. The underlying deposits (LF4) are eroded to a certain extent, forming erosional channels. The development of traction structures (LF5, LF6 and LF7) at the bottom of the single sand bodies is indicative of that strong channelised underflows and hydrodynamic conditions. Overall, the lower half of the single sand bodies are characterised by both lateral and downstream accretion. During the deposition of the top portion of the single sand bodies, hydrodynamic conditions decrease gradually. The widely developed massive and parallel stratification (LF8 and LF9) can be related to the aggradation by long-lived flows with high suspended loads (Camacho et al., 2002; Kneller & Branney, 1995). According to the conceptual schema associated with hyperpycnal systems proposed by Zavala et al. (2011), LF8 and LF9 are attributed to Facies S1 (suspended, massive sandstones) and Facies S2 (suspended, tabular fine-grained sandstones), respectively. These indicate river mouth deposits continuously fed by a long-lasting, fluctuating, and dilute turbulent flow (Mutti et al., 1996; Zavala et al., 2011).

Therefore, this FA is indicative of the development of underwater distributary channels at the delta front.

4.4 | Facies association 4

4.4.1 | Description

Composed of moderate grey to dark grey, massive mudstone with planar laminated and discontinuous silt levels, FA4 is also possibly accompanied by slump structures (LF12, Figure 4l and LF13, Figure 4m,n). In this facies association, abundant well-preserved plant debris and mica remains are recognised. Additionally, this unit exhibits a few interbedded greenish-grey tuffs (Figure 4o) and gloss black coals. Like FA2, units of FA4 reaches thicknesses of up to a few metres. Although FA4 evidences remarkably similar characteristics to FA2, it differentiates due to its darker colour, higher concentrations and smaller plant debris, and a lower proportion of siltstones/sandstones.

4.4.2 | Interpretation

The moderate grey to dark grey colours suggest reducing conditions, while the fine grain size implies deposition from suspension in a low gradient setting (Miall, 1985; Paredes et al., 2009). Abundant plant debris and mica remain in mudstones are considered a diagnostic criterion for hyperpycnites (Zavala et al., 2011). Therefore, FA4 is interpreted as forming from the deposition of fine-grained suspension that may accompany the collapse of suspension. These deposits may be attributed to an interdistributary bay or muddy prodelta environment in river floods (Liu et al., 2022; Sparks et al., 1993).

4.5 | Facies association 5

4.5.1 | Description

Comprised principally of massive fine-grained sandstones or siltstones with a few interbedded mudstones,

FIGURE 4 Facies associations of P_2s_1 and P_2h_g in Longdong Region. Five principal facies associations are identified and delineated. According to the transport mechanism and grain size of sedimentary rocks, we selected following typical photos that can reflect the sedimentary structural characteristics: (a) Grey conglomerate with erosion surface. Well-rounded gravel composition over 2 cm in diameter can be observed. Well ZT2, P_2h_g , 5044.3 m; (b) Greyish-white conglomerate with gravels in imbricated sub-horizontal alignments. Well QT2, P_2h_g , 4728.6 m; (c) Greyish-white conglomerate with diffuse lamination. Well L2, P_2h_g , 4762.6 m; (d) Interbedded conglomerate and pebbly sandstone. Well QT4, P_2h_g , 4325.8 m; (e) Greyish-white pebbly sandstone with diffuse lamination. Well L2, P_2h_g , 4773.6 m; (f) Greyish-white coarse-grained sandstone with asymptotic cross stratification. Well L1, P_2s_1 , 4257.1 m; (g) Grey pebbly sandstone with rip-up mudstone clasts. Well L6, P_2s_1 , 4479.66 m; (h) Grey massive fine/medium-grained sandstone. Well L20, P_2s_1 , 3830.2 m; (i) Grey fine-grained sandstone with parallel lamination; Well Li54, P_2h_g , 3945.5 m; (j) Siltstone interbedded with fine-grained sandstone. Climbing ripples developed frequently. Well L6, P_2s_1 , 4748.34 m; (k) Siltstone interbedded with fine-grained sandstone. Lithological abrupt interface developed frequently. Well L8, P_2s_1 , 4328.9 m; (l) Interbedded siltstone and fine-grained sandstone. Well L16, P_2s_1 , 4088.2 m; (m) Dark grey siltstone with mica remained. Well Li55, P_2s_1 , 3712.0 m; (n) Dark grey mudstone with terrigenous plants. Well L3, P_2s_1 , 4078.72 m; (o) Thin layers of grey-green tuff, Well CT3, P_2s_1 , 3748.0 m.

FA5 unit thicknesses ranges from 0.2 to 0.8 m and has been subdivided into three distinct lithofacies: (1) LF10—composed of fine-grained sandstones with climbing ripples or wave ripples (Figure 4j), which commonly grades vertically with LF9. (2) LF11—composed of interbedded fine-grained sandstones and siltstones with a gradational contact between coarsening-upward unit and fining-upward unit (Figure 4k). (3) LF12—composed of planar laminations or wavy-bedded mudstones and siltstones, also observed in FA2 and FA4. By contrast, LF12 in FA5 units may be accompanied by a slump structure. Additionally, well-preserved plant debris and mica remains can be observed in the above three lithofacies.

4.5.2 | Interpretation

These deposits are generally controlled by both fluvial and lacustrine processes formed under low-energy hydrodynamics, occurring mainly on the distal delta front. These sandstones are interpreted to be related to traction plus fallout processes from waning turbulent flows with high suspended loads (Sumner et al., 2008; Zavala et al., 2011). The formation of both a coarsening-upward unit and fining-upward unit not only reflects the sustained nature of the flow but also serves as a key criterion for hyperpycnites identification (Bhattacharya & Mac Eachern, 2009; Kneller & Branney, 1995). Intercalations of micas and other allochthonous plant matter could also be used as a criterion to identify hyperpycnal flow (Bhattacharya & Mac Eachern, 2009; Mutti et al., 2000, 2003; Zavala et al., 2011). According to the conceptual schema associated with hyperpycnal systems proposed by Zavala et al. (2011), the sandstones or siltstones in FA5 are comparable with Facies S2 (suspended, fine-grained sandstones with planar lamination), S3 (suspended, fine-grained sandstones with climbing ripples) and S4 (suspended, massive siltstones).

Therefore, this FA is interpreted as having been deposited at the distal delta front, which may be due to the development of lobes or sheet sands in the sublacustrine hyperpycnal system.

5 | PETROGRAPHIC AND MINERALOGIC ANALYSES

5.1 | Detrital component and matrix

According to Folk's (1974) criteria, the sandstones studied here can be classified as sublitharenites (61.0% in P_2h_8 and 50.0% in P_2s_1), followed by minor litharenites and feldspatic litharenites, and are expressed as having

an average composition of $Q_{76.2}F_{4.9}L_{18.9}$ (Figure 5b). To discriminate critically the provenance type of the detrital component, the Qt-F-L and Qm-F-Lt triangular diagrams proposed by Dickinson and Suczek (1979) were used in this study. Almost all data points are concentrated in the recycled orogen provenances field (Figure 5c).

Detrital quartz is predominantly monocrystalline and displays some degree of dissolution, replacement and fracture-filling (Figure 6a). Most of quartz grains appear as blue to blue-violet under CL observations (Figure 6b) and occasionally chert grains may be present in some thin sections (Figure 6c). In addition, sporadic distribution of high-temperature quartz ($>573^\circ\text{C}$) is found in the conglomerate or pebbly sandstone with rich volcanic matrix. This type of quartz has the following characteristics (Figure 6d,e): irregularly shaped, with delicate sharp edges; clean surfaces; corroded embayments; no wavy extinction; and smaller grain size than detrital quartz. The rare residual feldspar exhibits carlsbad-albite compound twinning under orthogonal polarisation (Figure 6f). Replaced plagioclase minerals can often be identified by the preservation of a faint grain outline. Rock-fragment content is greatly variable, ranging from 3.85% to 89.36%. The main type is quartzite with crenulated sub-grain boundaries (Figure 6g), followed by extrusive rock, mica and sedimentary rock (Figure 6h). It's worth noting that calcite or argillaceous clasts are also common. Due to the presence of feldspar remnants inside these clasts, we believe that they are formed by the alteration and replacement of feldspar (Figure 6i).

The detailed micro-characterisation by microscope allowed the recognition of three categories of VMS types A, B and C, abbreviated to VMSA, VMSB and VMSC through the documentation of content and existence of volcanic matrix. Petrographic summary is shown in Table 1 and Figure 7.

5.2 | Detrital texture

5.2.1 | Description

There is a significant difference in microtexture among the three types of VMS. VMSA samples has the highest proportion of gravel and mean grain size, but with the poorest sorting characteristics. Due to the occurrence of massive volcanic ash matrix, point contact and line contact dominate with barely any concavo-convex grain contact. By contrast, the VMSB and VMSC samples consist of moderate to well-sorted

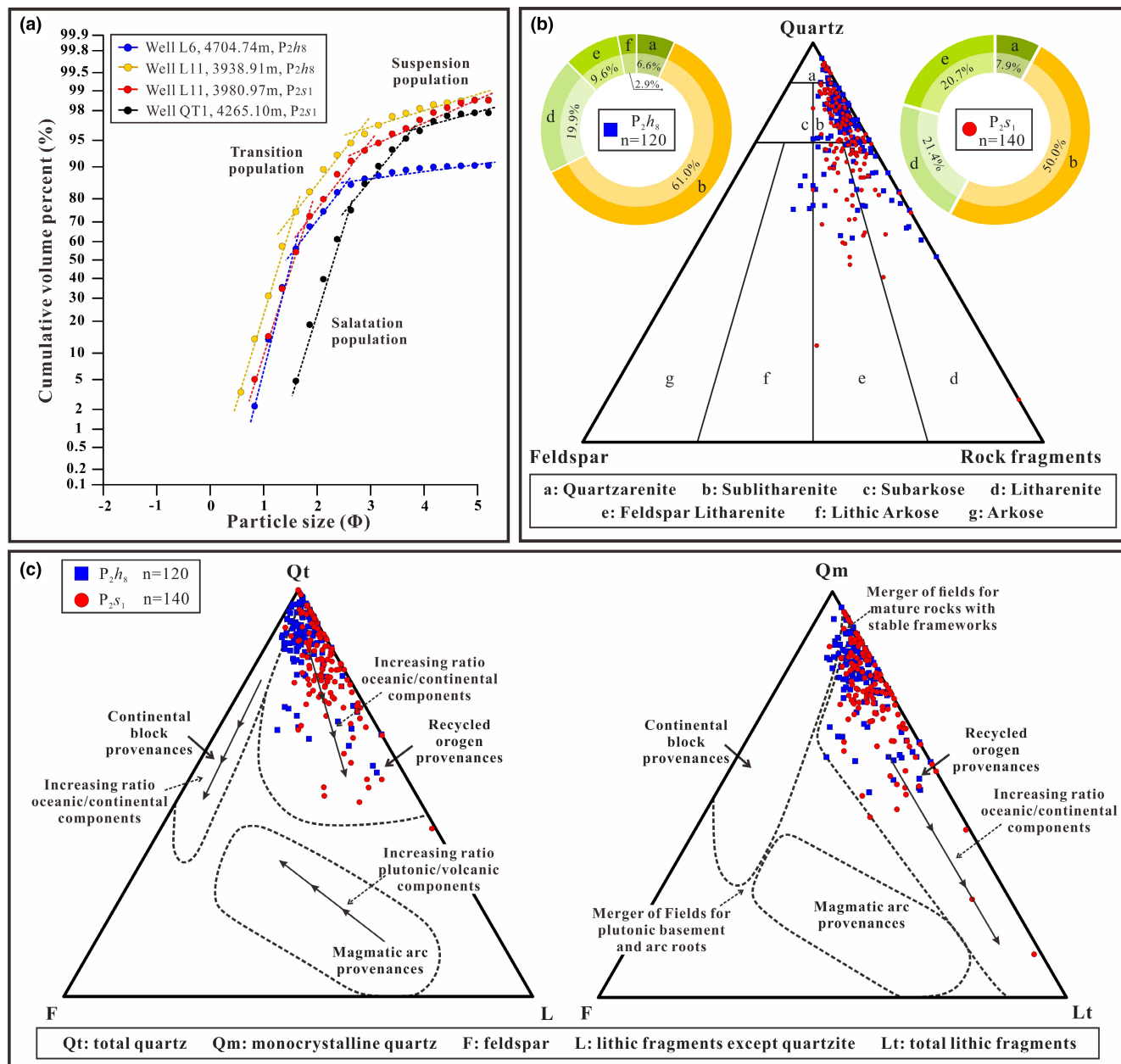


FIGURE 5 (a) Sediment transport dynamics to populations and truncation points in a grain-size distribution as revealed by cumulative grain size frequency curves. (b) Q-F-R triangular diagram of sandstone petrography showing the composition of P₂s₁ and P₂h₈ sandstones. (c) Qt-F-L and Qm-F-Lt triangular diagrams proposed by Dickinson and Suczek (1979) labelling the P₂s₁ and P₂h₈ sandstone composition data.

and sub-angular to sub-rounded grains, with significantly improved textural maturity. The cumulative grain size frequency curves of the four VMSA river mouth deposit samples show a three-stage pattern, corresponding to saltation population, transition population and suspension population (Figure 5a). The saltation population is between 55% and 75%, and the grain size is generally above medium-grained sand. The content of transition population is between 20% and 25%, and transport mode between saltation and suspension. The suspension population is between 5% and 15%.

5.2.2 | Interpretation

The high proportion of gravel and the mean grain size of VMSA indicates that the deposition of VMSA is under stronger hydrodynamic conditions. A poorly sorted VMSA is the result of rapid deposition and consolidation without sufficient mechanical differentiation. The result of the cumulative grain size frequency curves presents distinct traction current deposit characteristics. Hydrodynamics laws suggest that matrix compositions should not be deposited during the same time as sand-graded detrital component in normal flow (Worden & Morad, 2003). The formation

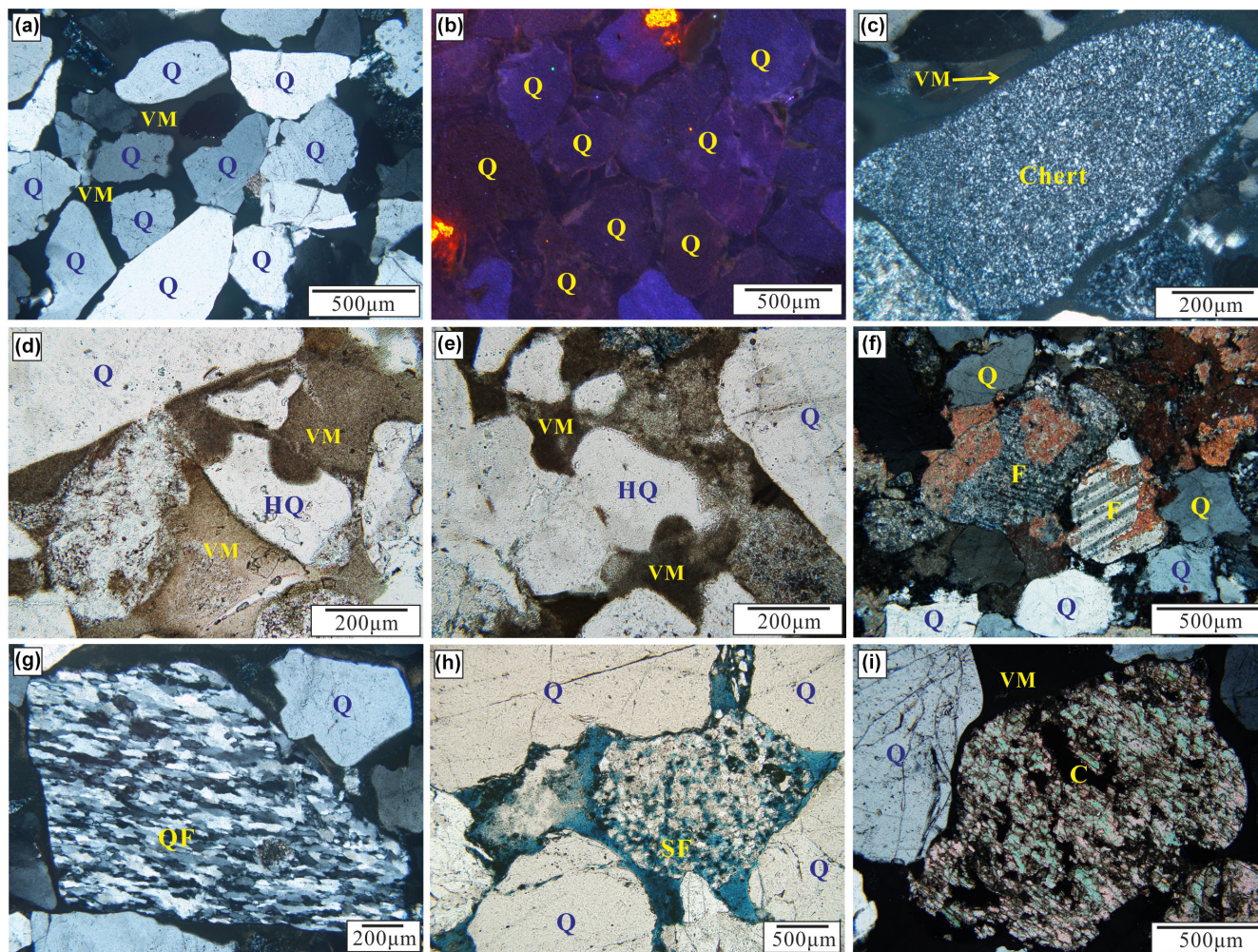


FIGURE 6 Typical microscopic images of terrigenous clastic grains in VMS. (a) Monocrystal quartz grains. Well QT3, P_2S_1 , 4240.0 m, XPL. (b) Most of quartz grains appear as blue to blue-violet under cathodoluminescence observations. Well L16, P_2S_1 , 4080.1 m, CL. (c) Coarse-grained chert. Well L22, P_2h_8 , 3550.5 m, XPL. (d) Fine-grained high-temperature quartz. Well QT3, P_2S_1 , 4240.0 m, PPL. (e) Fine-grained high-temperature quartz. Well QT3, P_2S_1 , 4240.0 m, PPL. (f) Residual feldspar exhibits carlsbad-albite compound twin. Well L7, P_2h_8 , 4155.2 m, XPL. (g) Quartzite fragment gravel. Well QT3, P_2S_1 , 4240.0 m, XPL. (h) Partially dissolved sedimentary fragment. Well Li54, P_2h_8 , 3949.2 m, PPL. (i) Carbonate clasts of completely replacement origin. Well L6, P_2h_8 , 4707.5 m, XPL. C, carbonate clasts; CL, cathodoluminescence; F, feldspar; HQ, high-temperature quartz; PPL, plane-polarised light; Q, quartz; QF, quartzite fragment; SF, sedimentary fragment; VM, volcanic matrix; XPL, cross-polarised light.

of VMSA must be induced by some particular hydrodynamic conditions (e.g., strong tidal current, turbidity current, debris flow and hyperpycnal flows) (Shchepetkina et al., 2018). We suggest VMSA could represent the peak period of flood or volcanic events, while VMSC represents the deposits of intermittent periods.

5.3 | Spatial distribution of volcanic matrix

To judge the location of volcanism relative to the study area, all the thin sections were identified and the contents of primitive volcanic matrix and clay minerals (kaolinite

and chlorite) altered by volcanic ash were statistically analysed. Although the study may be limited by sampling points, the results still reveal a trend (Figure 8). The mapped distributions of matrix content from single P_2S_1 wells ranges from 3.6% to 11.5%, with an average of 9.4%. The average content of the volcanic matrix, kaolinite and chlorite is 6.9%, 1.7% and 0.8%, respectively. Overall, there is seen to be an obvious reduction in volcanic matrix abundance in a northwestern direction, which is consistent with the direction of the paleocurrent (Figure 8a). The mapped distributions of matrix content from single P_2h_8 wells ranges from 5.9% to 23.5%, with an average of 12.6%. The average content of volcanic matrix, kaolinite and chlorite is 9.0%, 2.7% and 0.9%, respectively (Figure 8b),

TABLE 1 Petrographic summary of three types of VMS from the Upper Palaeozoic P_{2S1} and P_{2J8} in the Longdong Region

Type	VMSA			VMSB			VMSC			Total	
	Max	Min	Ave	Max	Min	Ave	Max	Min	Ave	Max	Ave
Detrital grains, %											
Quartz (monocrystalline)	76.50	15.00	55.24	86.00	39.00	66.34	86.50	10.00	70.51	64.60	64.60
Feldspar	12.00	0.00	1.41	11.00	0.00	0.59	12.00	0.00	0.80	0.79	0.79
Mica	10.00	0.00	1.23	8.00	0.00	1.01	2.00	0.00	0.41	0.98	0.98
Sand-size replaced kaolinite	7.00	0.00	1.43	12.00	0.00	1.60	8.50	0.00	0.86	1.46	1.46
Carbonate fragment	8.00	0.00	0.84	8.00	0.00	1.41	6.00	0.00	1.33	1.28	1.28
Metamorphic rock fragment											
Quartzite	15.00	0.00	5.10	30.00	0.00	4.67	67.50	1.00	7.84	5.19	5.19
Chert	4.00	0.89	0.00	5.00	0.00	1.15	2.00	0.00	0.99	1.08	1.08
Slate, phyllite, and schist	20.00	0.00	4.01	16.50	0.00	3.77	15.00	0.00	2.04	3.59	3.59
Others	7.00	0.00	2.26	6.50	0.00	1.66	3.50	0.00	1.26	1.73	1.73
Sedimentary rock fragment	3.00	0.00	0.06	4.00	0.00	0.21	1.00	0.00	0.09	0.18	0.18
Volcanic rock fragment	18.00	0.00	3.97	16.00	0.00	3.12	5.50	0.00	1.70	3.11	3.11
Interstitial material, %											
Altered volcanic matrix	39.00	15.50	21.62	15.00	5.50	10.09	5.00	0.00	4.14	11.69	11.69
Diagenetic components											
Carbonate cements	7.00	0.00	1.04	17.00	0.00	2.28	28.00	0.00	4.16	2.27	2.27
Siliceous cements	3.00	0.00	0.34	8.00	0.00	1.80	10.00	0.00	3.64	1.74	1.74
Ferruginous cements	10.00	0.00	0.37	5.00	0.00	0.25	8.00	0.00	0.23	0.27	0.27
Visible porosity, %	3.00	0.00	0.45	9.00	0.00	0.69	6.50	0.00	1.07	0.69	0.69
Brief descriptions	Volcanic matrix is filled in basal or full-pore type, which are mostly black or black brown under plane-polarised light.			Volcanic matrix only occupies part of the pores. Kaolinite, carbonate or siliceous cements can be observed accompanied by volcanic matrix, and the formation of these cements is closely related to the volcanic matrix alteration			The content of volcanic matrix is low. Such sandstones are spatially adjacent to VSMA & VSMB. The formation of authigenic minerals is probably related to the alteration and migration of volcanogenic materials in the adjacent VSMA and VSMB			-	

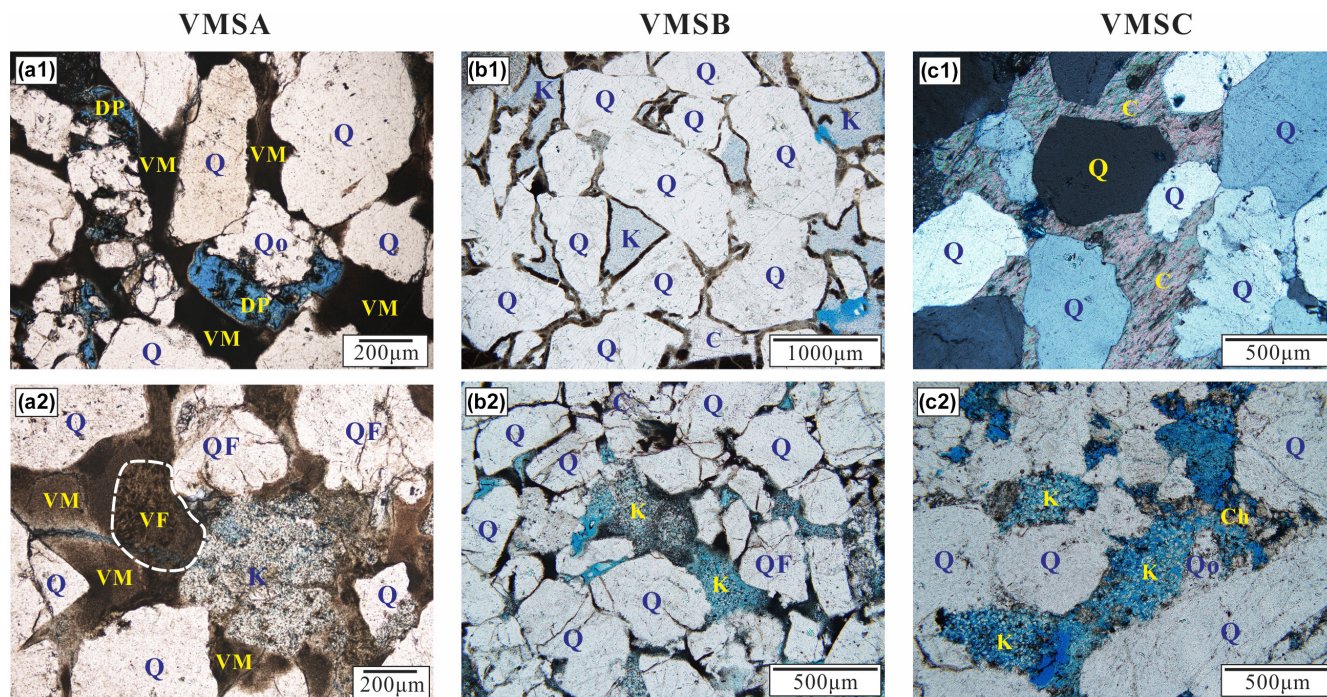


FIGURE 7 Typical microscopic photos of the three types of VMS. (a1) Volcanic matrix fully filling the pore space between clastic grains. The volcanic matrix is the collection of dust-like materials, which are mostly black or black brown. Well QT2, P_2h_8 , 4729.48 m, PPL. (a2) Volcanic matrix fully filling the pore space between clastic grains. The dark fine-grained pseudomatrix can be observed in the dusty collection, which may be the result of alteration of volcanic grains thermodynamically unstable. Well QT3, P_2s_1 , 4236.6 m, PPL. (b1) Volcanic matrix is distributed as detrital grain coats, thickness between 10 and 100 μm . Well L22, P_2h_8 , 3550.5 m, PPL. (b2) Volcanic matrix is scattered in the non-connected pore edge and throats. Well QT3, P_2s_1 , 4242.55 m, PPL. (c1) Primary intergranular pores are abundant with carbonate cements and the content of volcanic matrix is low. Well Li54, P_2h_8 , 3952.28 m, XPL. (c2) Primary intergranular pores are abundant with kaolinite cements associated with volcanogenic material alteration. Well QT1, P_2s_1 , 4267.6 m, PPL. C, carbonate cements; Ch, chlorite; DP, dissolved pores; K, kaolinite; PPL, plane-polarised light; Q, quartz; QF, quartzite fragment; Qo, quartz overgrowth; VF, volcanic fragment; VM, volcanic matrix; XPL, cross-polarised light.

with abundance also gradually decreasing towards the northwest. Vertically, VMS are mainly developed at the bottom of P_2h_8 and P_2s_1 , as shown in Figure 8c. The distribution of volcanogenic materials is rare elsewhere in these two members.

5.4 | Authigenic phases

Microscopic observation revealed that authigenic minerals formed in post-depositional conditions mainly include kaolinite, chlorite, siliceous and carbonate minerals.

5.4.1 | Clay minerals phase

Three types of kaolinite were identified in this study: (1) 'Clean' cement occurring in open pore spaces (shorthand for C-kaolinite, mostly in VMSC) (Figure 9a). Loose accumulation between crystals and abundant intercrystalline pores are developed internally. (2) 'Dirty'

cement associated with volcanic matrix (shorthand for D-kaolinite, mostly in VMSA and VMSB) (Figure 9b). D-kaolinite and volcanic matrix exhibit a mutual transition under microscopic observation, and there is ferruginous cementation residue inside the kaolinite aggregates after volcanic matrix alteration. The crystal size and intergranular pore development of D-kaolinite are obviously worse than that of C-kaolinite. (3) Sand-size replacement of feldspar grains or volcanic rock fragments (shorthand for R-kaolinite, mostly in VMSA) (Figure 9c). R-kaolinite aggregates maintain a good host grain shape, and it is almost impossible to identify the primary minerals. R-kaolinite is extremely closely arranged and completely encapsulated by the volcanic matrix. All types of kaolinite present as an azure blue light under cathodic luminescence (Figure 9b).

Chlorite, as acicular single crystals or aggregates, is dispersed in the volcanic matrix between clastic particles (Figure 9d,e), sometimes mixing with D-kaolinite. Its average content, however, is less than that of D-kaolinite. By contrast, chlorite filling in the pores of VMSC (e.g.,

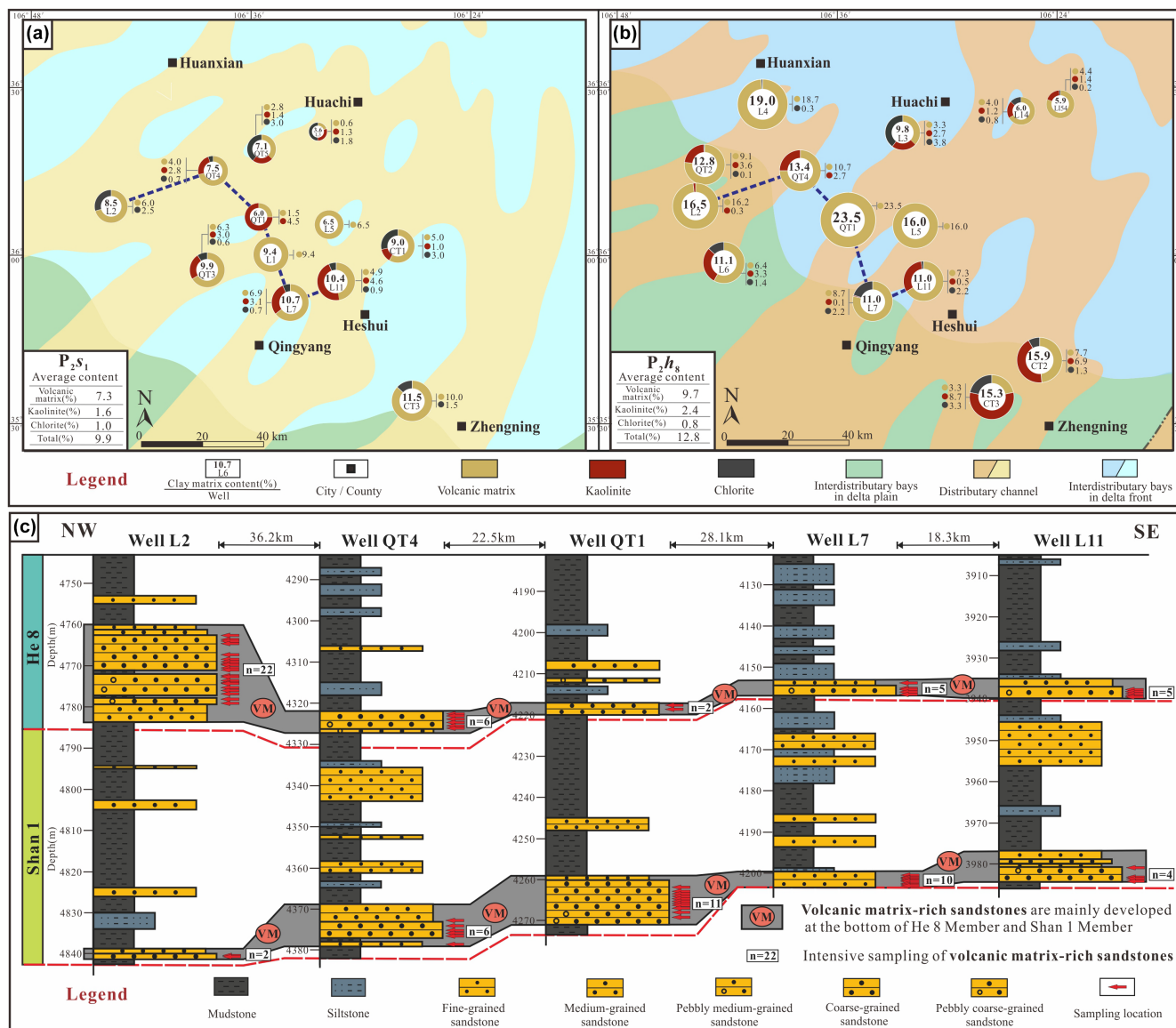


FIGURE 8 Spatial distribution characteristics of volcanic matrix content. (a) The mapped distributions of volcanic matrix in P₂S₁. (b) The mapped distributions of volcanic matrix in P₂h₈. (c) The vertical distribution of volcanic matrix in P₂S₁ and P₂h₈. VMS are mainly developed at the bottom of P₂S₁ and P₂h₈.

primary intergranular pores and mould pores) is relatively rare.

5.4.2 | Siliceous minerals phase

Siliceous cements are found in the form of quartz overgrowth and authigenic quartz crystal. In the VMSA samples, the mould pores formed by dissolution of feldspar or volcanic rock debris provided space for the growth of siliceous cements. Ordered microquartz crystals grew at the contact points between host grains and the surrounding quartz (or quartzite debris) grains. Quartz overgrowths then formed inward from the mould pore rims, which

appears to be controlled by the orientation of the pore margin shape (Figure 9f). The quartz overgrowth edges are locally blocked by authigenic kaolinite or carbonate cements. In VMSB, where volcanic matrix is present as detrital grain coatings, the siliceous cements are distributed throughout the pores in the form of polycrystalline authigenic quartz, varying from 10 to 200 μm in size (Figure 9g). For the samples in which the volcanic matrix is scattered and the pore rims and throats unconnected, the volcanic matrix cannot have been completely wrapped by the clastic particles, and the siliceous cements grow in the form of quartz overgrowth. In VMSC, the content of quartz overgrowth is much larger than that of VMSA and VMSB. The maximum cumulative thickness of quartz

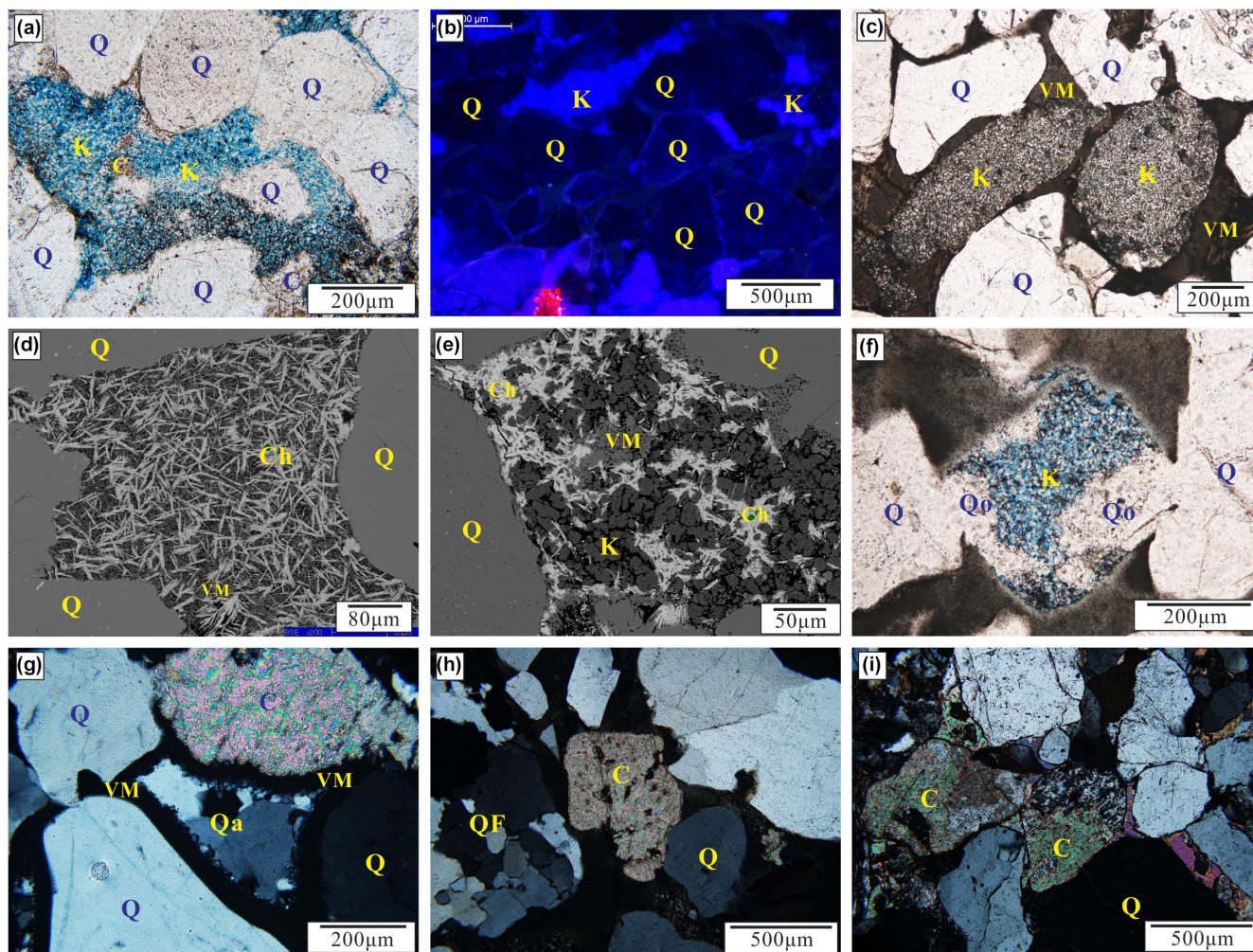


FIGURE 9 Typical microscopic photos of authigenic minerals phase. (a) C-kaolinite cements in the open pore spaces. Well CT3, P_2h_8 , 3725.1 m, PPL. (b) Kaolinite is present as azure blue light under cathodic luminescence. Well CT3, P_2h_8 , 3724.84 m, CL. (c) D-kaolinite is replaced by feldspar grains or volcanic rock fragments. Well QT3, P_2s_1 , 4236.6 m, PPL. (d) Acicular single-crystal chlorite is dispersed in the volcanic matrix. Well CT3, P_2h_8 , 3728.9 m, BSE. (e) Chlorite aggregate mixed with D-Kaolinite is dispersed in the volcanic matrix. Well QT2, P_2h_8 , 4735.9 m, BSE. (f) Quartz overgrowth grows inward from the mould pore rims. Well QT2, P_2h_8 , 4735.9 m, PPL. (g) Polycrystalline authigenic quartz. Well L22, P_2h_8 , 3550.5 m, XPL. (h) Carbonate minerals are formed by the replacement of detrital grains. Well L4, P_2s_1 , 4498.4 m, XPL. (i) Carbonate minerals formed by replacement of detrital grains and cementation. Well L7, P_2h_8 , 4155.2 m, XPL. BSE, back scattering; C, carbonate cements; Ch, chlorite; CL, cathodoluminescence; K, kaolinite; PPL, plane-polarised light; Q, quartz; Qa, polycrystalline authigenic quartz; QF, quartzite fragment; Qo, quartz overgrowth; VM, volcanic matrix; XPL, cross-polarised light.

overgrowth can reach $200\mu\text{m}$, accompanied by multiple dust rims, and there is ‘healing’ phenomenon between clastic quartz grains.

5.4.3 | Carbonate minerals phase

Carbonate cements occur in two forms: where the detrital grain is replaced (in all three types of VMS) and intergranular filled carbonate minerals (mostly in VMSC). In VMSC, the detrital grains are completely replaced by carbonate minerals, and the optical characteristics of the host grains can barely be distinguished under the

microscope (Figure 9h). However, in VMSC, the residual structure of feldspar, volcanic rock fragments and chert can be observed after replacement (Figure 9i). These differences indicate that the volcanic matrix content may have an effect on the formation of carbonate minerals to some extent. Under CL observation, azure blue kaolinite crystals can be observed inside the bright orange carbonate minerals, indicating that the carbonate minerals can have been replaced by kaolinite. For intergranular cements, early carbonate cements in the form of basal cementation and late carbonate cements growing inside quartz grain fractures and outside of quartz overgrowth can be observed.

6 | BULK-ROCK GEOCHEMISTRY

6.1 | Elemental composition of matrix

6.1.1 | Major element oxides

The volcanic matrix mainly appears as a stubby cryptocrystal aggregate with the major compound SiO₂ accompanied for example by small amounts of Al₂O₃, FeO and MgO (Figure 10). The single crystal diameters are evenly distributed at around 1 μm, and the average content of SiO₂ can reach more than 95%. Cryptocrystalline titanium oxide often occurs inside volcanic matrix (Figure 10d). Because these cryptocrystalline minerals appear brighter in the BSE images, they can be clearly distinguished from the volcanic matrix. They are irregularly dispersed in quartz cryptocrystal aggregates and poorly low in abundance, which may be due to the anatase being of authigenic origin.

6.1.2 | Trace elements

The La-Th-Sc, Th-Co-Zr/10 and Th-Sc-Zr/10 triangular diagrams proposed by Bhatia and Crook (1986) were used in this study for six tuffaceous interlayer samples. On the La-Th-Sc tectonic discriminate diagrams, four samples fall within the field of active continental margin and passive margin and two samples fall on the boundary line. On the Th-Co-Zr/10 tectonic discriminate diagrams, all six tuff samples fall on the edge of active continental margin field. On the Th-Sc-Zr/10

tectonic discriminate diagrams, four samples fall within the field of active continental margin and two samples within continental island arc (Figure 11a). The analyses for six samples of tuffaceous interlayer are displayed on a Floyd and Leveridge (1987) plot of Zr/TiO₂ versus Nb/Y (Figure 11c). Three samples fall within the trachyandesite field, two samples within rhyodacite dacite field, and one sample falls on the boundary between rhyodacite dacite and trachyandesite field. Refer to Appendix A for all sample information.

6.1.3 | Rare earth elements

The rare earth elements pattern standardised by the Upper Continental Crust (UCC) shows a relatively consistent pattern for the six tuffaceous interlayer samples: The samples are enriched in light rare earth elements (LREE) with an average content of 187×10^{-6} to 582×10^{-6} ppm, and depleted in heavy rare earth elements (HREE) with an average content of 45×10^{-6} to 129×10^{-6} ppm. The LREE/HREE value is about 5, indicating the differentiation between LREE and HREE. All samples show negative Eu anomalies ($\delta\text{Eu} = 0.63\text{--}0.83$) and no Ce anomalies (Figure 11b). Refer to Appendix A for all sample information.

6.2 | Fluid inclusions data

Fifty aqueous inclusions in five samples were found and their homogenisation temperatures and salinities were

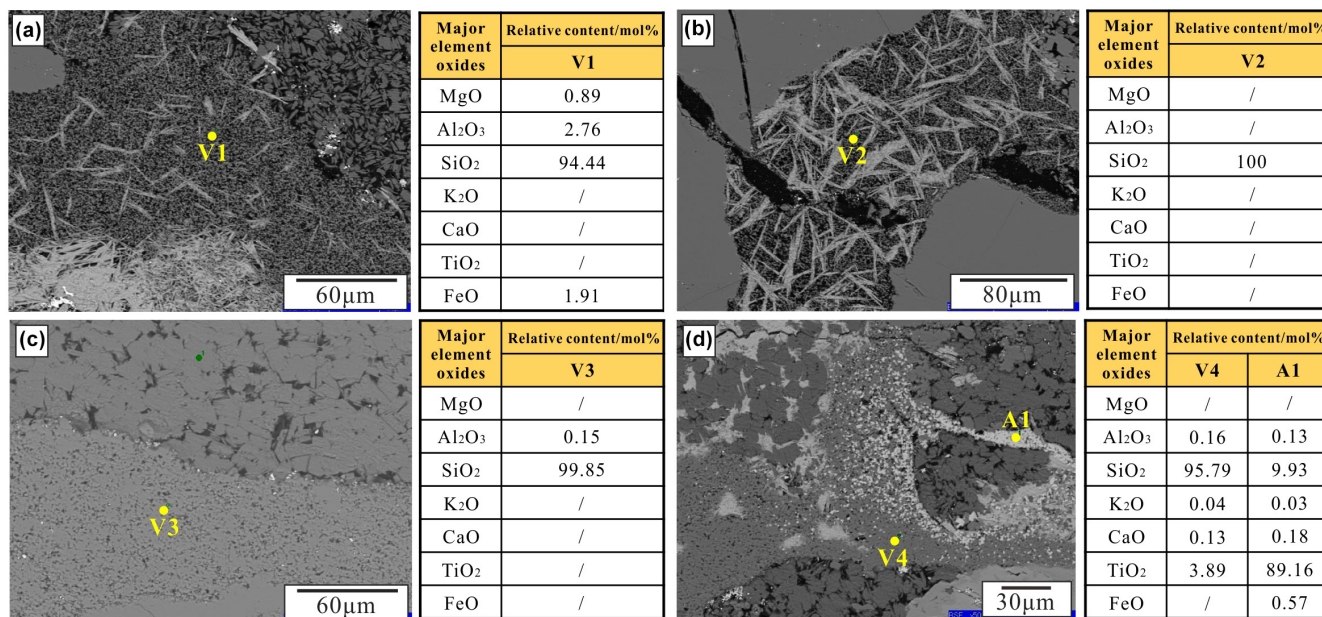


FIGURE 10 Photomicrographs and chemical compositions of volcanic matrix. Yellow solid circles show the portion analysed by electron microprobe. (a) Well CT3, P₂h₈, 3728.9 m. (b) Well CT3, P₂h₈, 3728.9 m. (c) Well L6, P₂h₈, 4707.5 m. (d) Well QT3, P₂S₁, 4236.6 m.

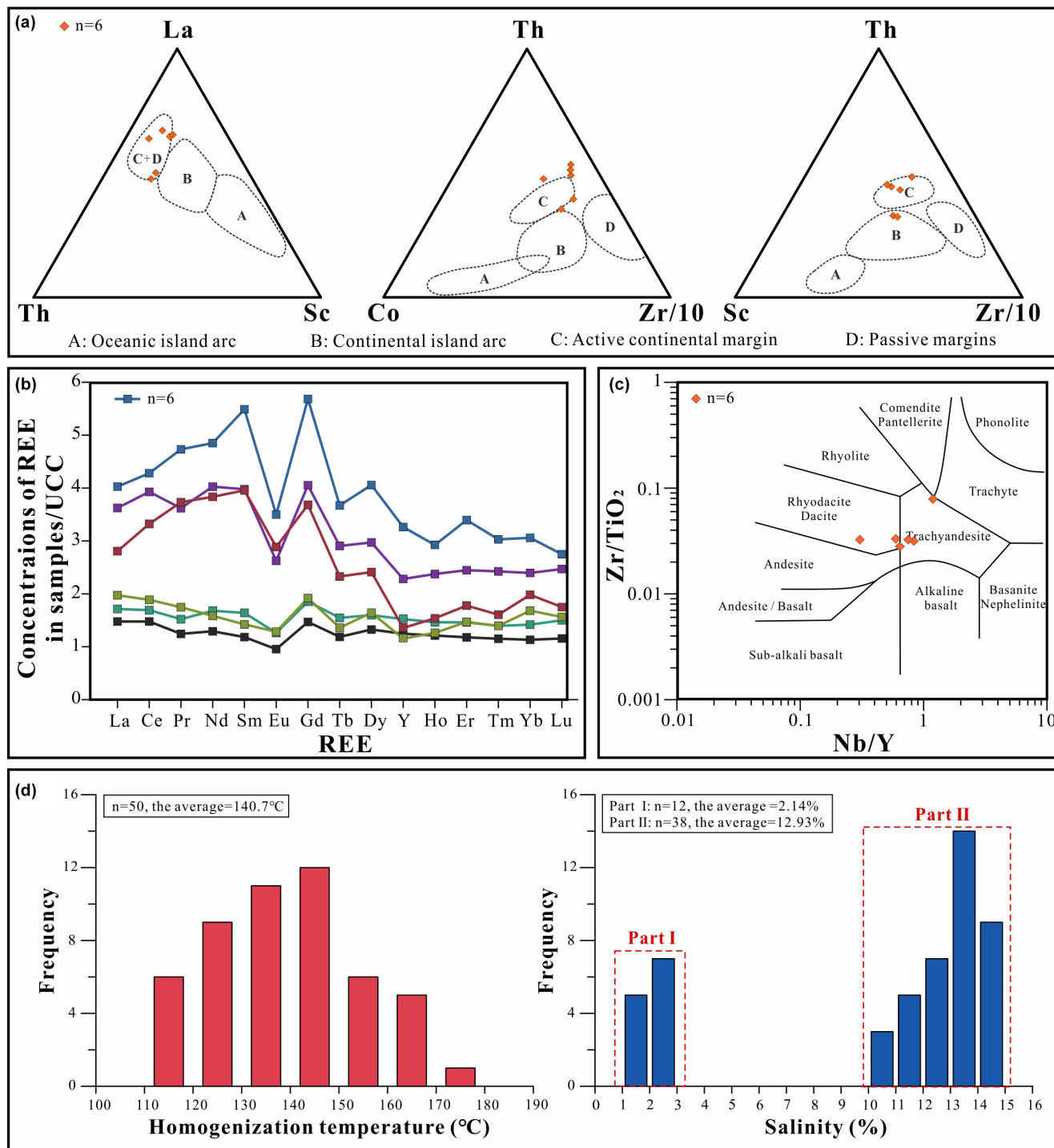


FIGURE 11 (a) La-Th-Sc, Th-Co-Zr/10, Th-Sc-Zr/10 tectonic-setting discrimination plot (after Bhatia & Crook, 1986). (b) The rare earth elements pattern was standardised by the Upper Continental Crust (UCC) of six tuff samples. (c) Zr/TiO₂ vs. Nb/Y diagram (after Floyd & Leveridge, 1987) shows the volcanic matrix was derived from Rhyodacite Dacite and Trachyandesite. (d) Histogram of the homogenisation temperature and salinity for the aqueous inclusions in quartz overgrowth.

measured (Refer to Appendix B for sample information and details). Homogenisation temperatures have a relatively concentrated distribution range (from 118 to 180°C), with most ranging from 120 to 150°C and an average of 140.7°C (Figure 11d). Correspondingly, the distribution

range of salinity is large, with two distinct intervals. The salinity of 12 fluid inclusions ranges from 1.74 wt% NaCl to 2.57 wt% NaCl (mean value is 2.14 wt% NaCl), and the salinity of 38 fluid inclusions ranges from 10.90 wt% NaCl to 14.18 wt% NaCl (mean value is 12.93 wt% NaCl).

7 | DISCUSSION

7.1 | Why are the matrix components judged to be the result of volcanic ash alteration?

The volcanic origin of matrix components can be determined from the following information of bulk-rock geochemistry and petrology: (1) In the matrix-rich sandstones of lacustrine and fluvial deposits, the matrix components mainly consist of an irregular mixing of clay minerals (smectite and illite/smectite mixed layer) and silty grains (Hower et al., 1999; Worden & Morad, 2003). However, the matrix components in VMSA are mainly pure stubby cryptocrystal quartz aggregates (Figure 10), which may indicate that their origin was due to abnormal sources and transport mechanisms caused by sudden geological events. (2) Ti is usually considered to be less susceptible to migrate during volcanic glass alteration because of low solubility in low-temperature aqueous solutions (Kipli et al., 2017; Zielinski, 1985). This characteristic makes titaniferous minerals suitable for identifying the origin of volcanic matrix (Figure 10d). (3) A negative Eu anomaly requires extreme reduction and high-temperature conditions (Cullers, 2000), which is commonly found in magmatic settings rather than in surficial environments (Dai et al., 2017; Rard, 1985). Therefore, the existence of volcanogenic materials could be reflected by the degree of the negative Eu anomaly (Cullers, 2000), which is also of great significance in determining the origin of magmatic rocks of matrix components (Figure 11b) (Burger et al., 2002; Hower et al., 1999). (4) High-temperature quartz can also be used to indicate the source of volcanogenic materials (Dai et al., 2017). High-temperature quartz is common in VMSA (Figure 6d,e), but hardly observable in VMSB and VMSC. Therefore, it is likely to be transported into the sediments along with the matrix, rather than with terrigenous clastic quartz.

7.2 | Were widespread volcanogenic materials attributed to a single origin as previously thought?

It is widely held that the provenance of detrital particles mainly derived from the NQOB occurred during the Late Palaeozoic in the study area (Figure 5c) (Dong et al., 2011; Dong & Santosh, 2016). However, scant studies are concerning the volcanic matrix of the sediments. Due to the collision between the Central Asian Orogenic Belt and the northern margin of Ordos Basin, intensive magmatism occurred between ca. 340–320 Ma and ca. 285–260 Ma in the YYOB (Fan et al., 2019; Yang et al., 2006). This has

led to the misconception that the volcanogenic materials throughout the basin were attributed to a single YYOB origin. If the volcanic matrix of the Longdong Region was derived from the YYOB, the sediments in the northern Tianhuan Depression (Figure 1a) should also contain higher volcanogenic materials. However, Zhu et al. (2020) conducted a detailed investigation on the petrology of P_2s_1 and P_2h_8 in the northern Tianhuan Depression and found the matrix was dominated by detrital illites (with an average of approximately 4%) and mica flakes (with an average of approximately 1%). Volcanic matrix content is very low and alteration characteristics are completely different from those in the Longdong Region. Therefore, we question the view that the volcanogenic materials were derived from the northern margin of the basin.

Previous studies have shown that there are detrital zircon age groups of Carboniferous and Permian in the P_2s_1 and P_2h_8 of the Southern Ordos Basin (Appendices C, D and E). Because there are rarely reports on zircon U–Pb ages of Permian igneous rocks from the present outcropped magmatic rocks in the QOB, existing research has led to the conclusion that the detrital zircon age groups of Permian in Longdong Region can only be derived from YYOB (Liang et al., 2020). However, modern outcrops cannot be used to represent ancient provenance in source-to-sink studies. The lack of present Permian outcropped magmatic rocks in the NQOB might be the result of intensive and complete denudation. Moreover, existing research has shown that there is indeed evidence for Permian detrital zircon in the NQOB. Sun et al. (2013) also found 260 ± 3 to 269 ± 3 Ma granitic detrital zircon records in the western part of the NQOB, indicating that magmatic movement did exist during the sedimentary period of P_2s_1 and P_2h_8 . Evidence for these detrital zircon records were only recorded in the Permian and Triassic sediments derived from the NQOB in the south of Ordos Basin. We collected and collated the Triassic detrital zircon records in Appendix F. In addition, Jiang et al. (2020) compared 260–350 Ma zircons Hf isotopic compositions from the sediments in P_2s_1 and P_2h_8 in the southwestern margin with the YYOB by in situ zircon Lu–Hf analyses. The results showed that the $\epsilon_{\text{Hf}}(t)$ and the $T_{\text{DM}2}$ were significantly different from each other, and it was inferred that the provenance of ca. 350–260 Ma detrital zircons was not from the YYOB.

Based on the above evidence, we propose the hypothesis that there may have been magmatism in the Permian of NQOB and this volcanism provided volcanogenic materials for the P_2s_1 and P_2h_8 in the Longdong Region and formed widely developed VMS. However, intensified weathering and denudation occurred soon afterwards, resulting in detrital zircons only being recorded in the Permian and Triassic sediments. The lack of igneous

rock data from the present NQOB outcrop is also the result of intense and complete denudation during the Late Palaeozoic and Mesozoic. According to the discrimination results of trace elements, the volcanogenic materials are interpreted as intermediate-acidic origin, such as trachyandesite (Figure 11c). These volcanogenic materials may be built up by repeated, relatively small-scale eruptions and are typical of convergent plate margins with thick continental crust (Figure 11a) (Cronin et al., 1996; Lenhardt et al., 2011; Manville et al., 2009). This may be associated with continental lithosphere subduction generating asthenospheric circulation or remote effects of Mianlue oceanic crust subduction (Dong et al., 2011; Dong & Santosh, 2016). From the Late Palaeozoic to the Middle Triassic, the Ordos Basin was characterised by continuous deposition above the North China Craton. The interior of the basin has always been in a very stable tectonic state and does not have the conditions for the development of volcanic activity (Chen et al., 2021; Liang et al., 2020; Zhu et al., 2020). Therefore, the major volcanic centres tend to be located on the basin's edge, that is, towards the south or west of the Longdong Region as implied by the southwesterly thickening and increasing volcanogenic materials (Figure 8). Although the source of the volcanogenic materials was speculative, combined with the current geochronological data and geological background. It is still the most reasonable explanation.

7.3 | How can volcanic ash be mixed with terrigenous debris under long-distance transport?

7.3.1 | Identification of hyperpycnal flows

The following phenomena indicate that the volcanogenic materials in P_2s_7 and P_2h_8 were mainly deposited from fluvial process and not from air-fall: (1) The volcanogenic materials are usually associated with sandstone successions. However, the content of volcanogenic materials in non-main channel sedimentary environments is extremely low. (2) The air-fall volcanic ash can fill intergranular pores of clastic grains by matrix infiltration (Buurman et al., 1998; Worden & Morad, 2003), which is not possible for sand-size grains. Therefore, it is more likely that the pyroclastic pseudomatrix (Figure 8A2) and high-temperature quartz (Figure 6d,e) observed in the thin section of VMSA were transported by fluvial processes. (3) Virolle et al. (2018) demonstrated that the detrital grain coats of estuarine sediment are deposited at the same time as the sand grains under strong hydrodynamic conditions. Therefore, during the saltation or suspension

transportation in VMSB by fluvial process, volcanic matrix was constantly bound to the surface of sand grains.

Recognition of hyperpycnal flow at the river mouth mainly based on lithofacies associations is widely accepted by a number of scholars. According to the conceptual schema associated with hyperpycnal systems proposed by Zavala et al. (2011), Lithofacies 1 to Lithofacies 6 can be attributed to Facies B (Bed load) and Lithofacies 7 to Lithofacies 13 can be attributed to Facies S (Suspended load). These predictive facies are widely applied to the identification of sustained turbulent (noninertial) hyperpycnal flow deposits caused by flood events. Similarly, Mutti et al. (1996) proposed an idealised hyperpycnite succession formed in flood-dominated fluvio-deltaic settings. In their study, river mouth deposits followed Facies 6 (coarse-grained and channelised mouth bar deposit) and approximately Facies 7 (bar-slope deposit) and Facies 9 (fine-grained and thin-bedded sandstone lobes) from bottom to top, with individual thicknesses commonly between 5 and 15 m. The sedimentary sequence characteristics of VMS in the Longdong Region are remarkably similar to this model. In addition, this research has recognised that ancient hyperpycnites can be seen in the VMS, including inverse-to-normal grading (Mulder et al., 2003; Figure 4k), repeated traction structures in mudstone and siltstone (Wilson & Schieber, 2014, 2017; Figure 4j,l), massive sandstones (Steel et al., 2016; Figure 4h), and plant and mica remains (Zavala & Arcuri, 2016; Figure 4m,n).

Therefore, it is inferred that the sedimentary sequences associated with VMS were the result of the formation and development of an ancient hyperpycnal river-delta system. Given the triggering mechanism, two interpretations could be made: (1) Syn-eruptive hyperpycnal flow. Catastrophic paroxysmal eruption events can increase river density and flow energy, resulting in the formation and development of an ancient hyperpycnal river-delta system. Landslides triggered by volcanic eruptions can provide large amounts of sedimentary materials (Dadson et al., 2004; Ponciano & Della-Fávera, 2009). High-speed pyroclastic flows, lahars, levee breaches induced by volcanism could directly carry these materials into river systems, intensifying the fluid density difference at the river mouth and producing conditions conducive to triggering hyperpycnal flow. (2) Post-eruptive hyperpycnal flow. Volcanism occurred before the deposition of P_2s_1 and P_2h_8 VMS. During the syn-eruptive period, sedimentary processes occurred without a direct volcanic influence. Instead of being instantly washed into the river, the volcanogenic materials over a long period of geological history become available as a sediment source in the catchments. Subsequently, the rapid incorporation of large quantities of volcanic matrix accompanied with the terrigenous clastic being brought by hyperpycnal flow

occurred during the sedimentary period at the bottom of P_2h_8 and P_2s_1 . Extreme events, such as periodic precipitation, dam breaks, glacial outburst flood and earthquake may be the triggers causing hyperpycnal flows at the river mouths (Jin et al., 2021; Mulder et al., 2003).

7.3.2 | Reconstruction of depositional processes

7.3.2.1 | Quiescent period I

In freshwater lacustrine systems, the difference in density between incoming flow and water in the basin is small. In consequence, a homopycnal flow was widely developed. The concentration of volcanogenic materials was very low, making it difficult to observe the volcanic matrix composition in river mouth deposits, which formed the VMSC.

7.3.2.2 | Waxing period

The flow transported a part of the volcanogenic materials, resulting in the flow property conversion from homopycnal flow to low-density hyperpycnal flow (Figure 12). The volcanic matrix transported by the low-density hyperpycnal flow was not sufficient to completely fill the primary intergranular pores, thus forming the VMSB at the river mouth. With the increasing transport distance, the density and energy of flow would gradually decrease with the flow density dropping below the critical discharge threshold at the distal delta front. This process would elutriate the matrix components to form 'clean' sandy deposits, restoring the characteristics of VMSC.

7.3.2.3 | Quasi-steady hyperpycnal flow period

The flow capacity to transport terrigenous clastic and volcanic matrix reached its peak during this period. The deceleration of the hyperpycnal flow at river mouths, due to friction and mixing, led to deposition of the coarser-grained sediment within the matrix (Mutti et al., 1996). These high-efficient hyperpycnal flows had erosive potential, enabling them to erode the underlying bed (earlier sediments of VMSA and VMSB at the river mouth) (Petter & Steel, 2006). Subsequently, debris and matrix gradually or incrementally aggraded (Kneller & Branney, 1995) and formed VMSA. At the beginning of deposition, VMSA was in an unconsolidated state, and multiple episodes of matrix infiltration due to gravity resulted in a higher content of matrix in the coarse-grained sediments at the bottom. In the meantime, fine-grained sand and mud were transported into distal delta-front regions. As the hyperpycnal flow moved towards the lacustrine basin centre, the hydrodynamic conditions and flow density gradually decreased to the critical discharge threshold. Therefore, there was

a general trend of transition from VMSA to VMSB and VMSC towards the lacustrine basin centre (Figure 12).

7.3.2.4 | Waning period

As the volume, sediment concentration and momentum of flow decreased, the channels formed during the quasi-steady hyperpycnal flow period would be filled by sediments, forming a typical normal graded bed sequence, until channels were blanketed with VMSB. The grain grading and sedimentary structure in this period may be slightly different from that of the pre-eruption period, but the plane distribution of the types of VMS was similar.

7.3.2.5 | Quiescent period II

Finally, the river density entering lake basin was always below the critical discharge threshold, resulting in homopycnal flow to redevelop. The content of volcanic matrix transported by flow could be negligible, and the sediments were all VMSC.

7.4 | How did the volcanic matrix alter to form the authigenic minerals?

7.4.1 | Paragenetic sequence accompanied by volcanic matrix alteration

Diagenetic stages can be divided into Eodiagenesis (<85°C), Mesodiagenesis (85–175°C) and Telodiagenesis (>175°C) (Schmidt & McDonald, 1979) (Figure 13). The complexity of burial and diagenetic pattern and the limitations of sample selection make it difficult to determine precisely the timing and duration of diagenesis. Therefore, the determination of some paragenetic sequence may be speculative.

The most significant characteristics during the Eodiagenesis stage were carbonate cementation and the formation of chlorite matrix associated with the hydrolysis of volcanic ash. The dissolution of highly reactive volcanic glassy particles can occur with the participation of pore water and atmospheric fresh water (Fisher & Schmincke, 1984), and exert a strong influence on diagenetic processes (Murray et al., 2018). The first to be leached from the volcanic matrix are highly reactive elements such as Na, K, Ca and Fe (Stefansson & Gislason, 2001). The authigenic minerals related to Na and K generally have extremely high solubility, making it difficult for them to precipitate out and be preferentially released into the surrounding water. By contrast, Ca and Fe released from the volcanic matrix and plagioclase are more likely to be sealed into authigenic phases (Kastner & Gieskes, 1976; Longman et al., 2021). Murray

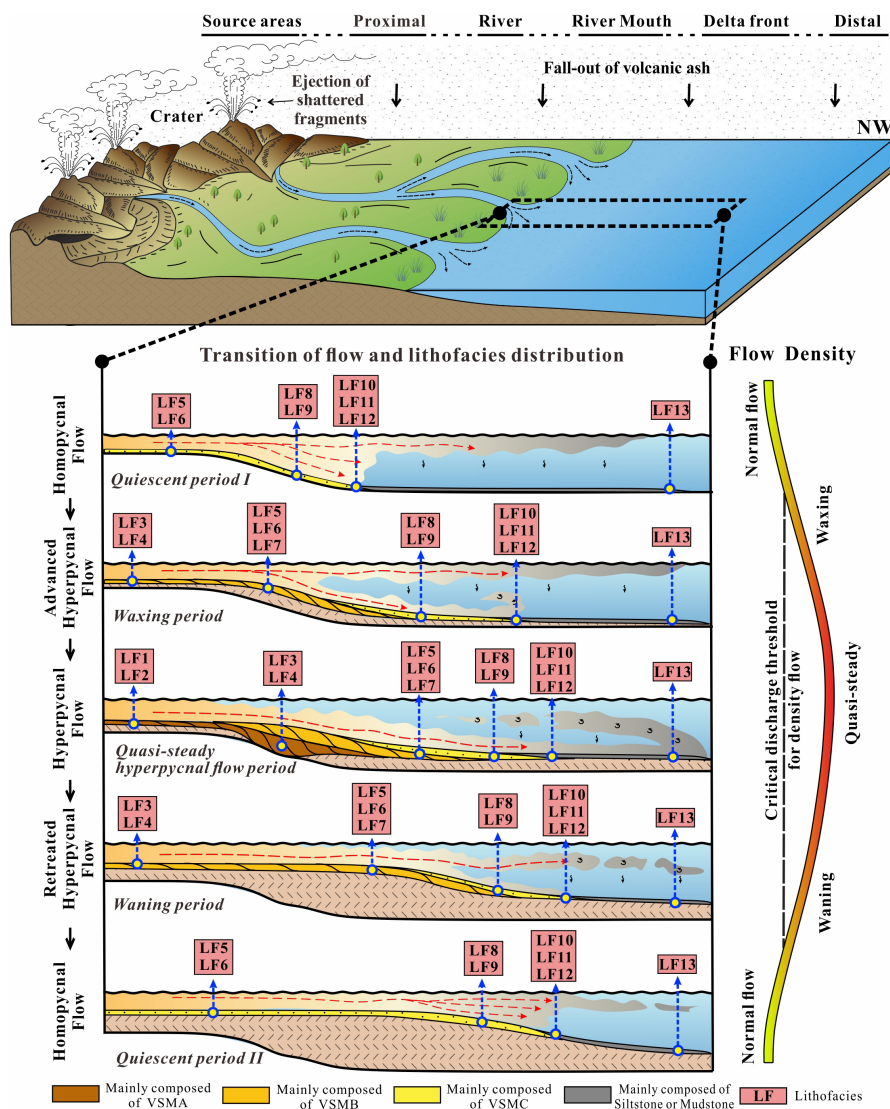


FIGURE 12 Idealised depositional sequence model for three types of VMS from the Upper Palaeozoic P_{2s1} and P_{2h8} in the Longdong Region. The depositional processes can be divided into five periods based on the variation of discharge. VMS is widely developed during the Quasi-steady hyperpycnal flow period at the river mouth.

et al. (2018) believed that the pore fluids are generally supersaturated with respect to calcite in tephra-rich sediments in shallow burial environments. The source of 'C' for carbonate cements probably resulted from the formation water and meteoric water (Zhu et al., 2019). They mostly have direct contact with detrital framework grains and developed prior to the precipitation of quartz overgrowth. Chlorite occurs more frequently in samples with basal or full-pore filling volcanic matrix. The poor initial physical property conditions restricted the discharge of iron and magnesium via hydrolytic alteration. Chlorite precipitated from the alkaline pore water when the ionic concentration reached the saturation phase (Anjos et al., 2003; Hillier et al., 2006; Ziegler, 2006). Therefore, the heterogeneity of physical properties

would lead to the uncertainty of iron and magnesium concentrations, which eventually lead to large discrepancies in the distribution of chlorite. Subsequent mechanical compaction resulted in further deterioration of physical property conditions, making it less susceptible to acidic fluids in the Mesodiagenesis stage (Carothers & Kharaka, 1978).

Mesodiagenesis stage was characterised by dissolution of volcanic matrix and feldspar, kaolinite cementation and siliceous cementation. Organic acid anions (carboxylic) typically dominate PH values in the fluid phase from 80 to 120°C and significantly affect aluminosilicates stability (Carothers & Kharaka, 1978). Therefore, feldspar experienced intensive dissolution at the early stage of organic acid discharge (starting around 80°C).

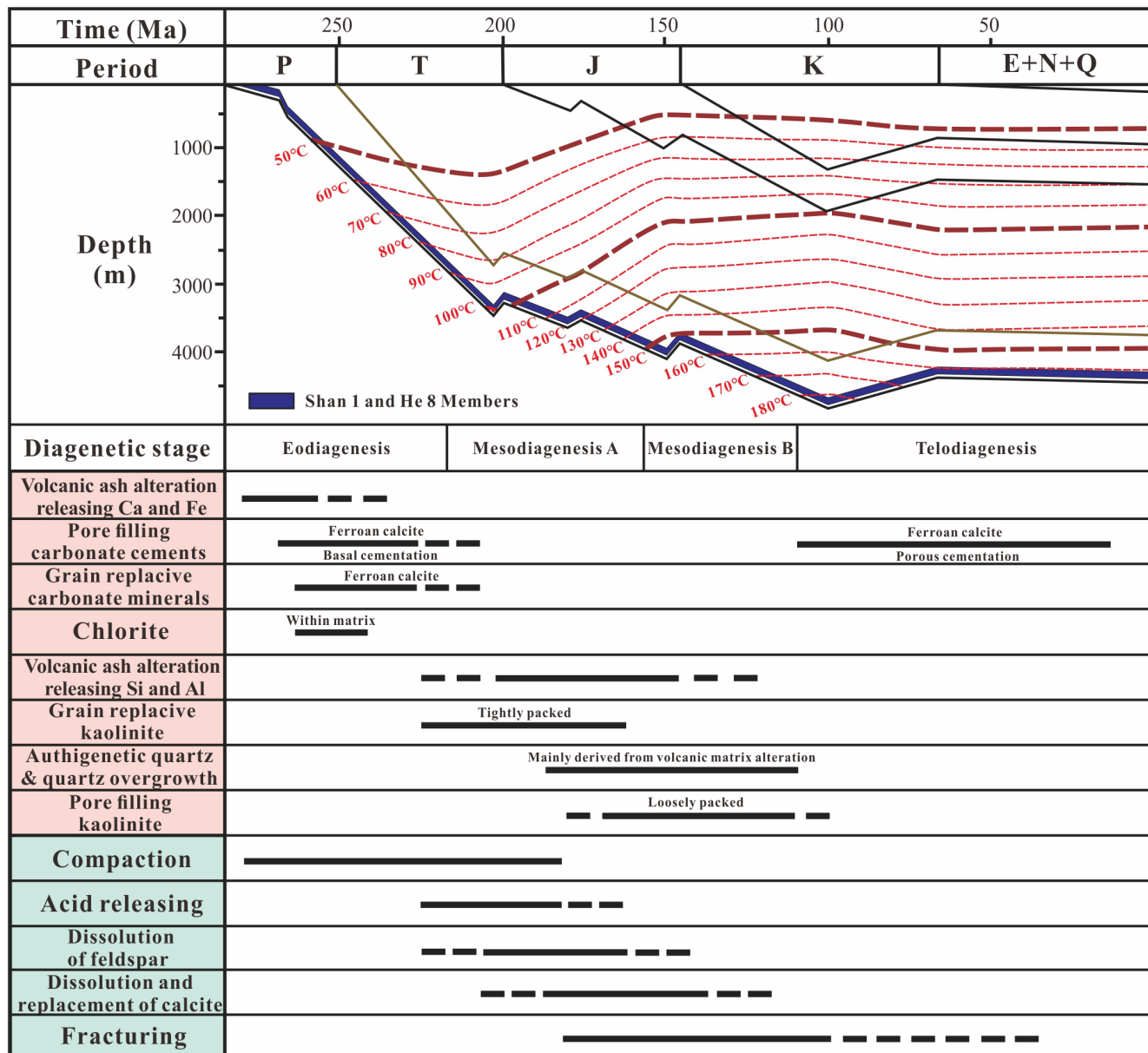


FIGURE 13 Paragenetic sequence established by the cross-cutting relationships, intergrowth relationships between the authigenic minerals and fluid-inclusion microthermometry data.

At temperatures greater than 100°C (mainly 120–160°C), the carboxylic acids begin to decarboxylate to form CO₂, increasing carbonate solubility (Franks & Forester, 1984). Post-dating dissolution, siliceous cements gradually precipitated according to the homogenisation temperature of inclusions from 110 to 180°C (Figure 11d). As volcanic matrix alteration progresses, the resulting amorphous silica-rich phase took up more space than the parent glass shard, resulting in alteration products migrating to the surrounding sediments (White et al., 2010). Hence, the siliceous source can most likely be explained by volcanic alteration. Because of the complex water-rock reactions in volcanogenic materials, alteration led to an increase

in fluid salinity resulting in most quartz overgrowth inclusions showing high salinity characteristics. The small amount of quartz inclusions with low salinity were probably formed by reprecipitation after pressure solution (Figure 11d). The pore filling kaolinite growing outside of the quartz overgrowth, and the presence of corroded carbonate crystals existing in the kaolinite aggregates indicates pore filling kaolinite postdated quartz overgrowth and early carbonate cements (Figure 9a). The widespread phenomenon of quartz overgrowth replacement by kaolinite indicates the same silica source or both (Zhu et al., 2020). The aluminium can also be derived from volcanic alteration or feldspar dissolution.

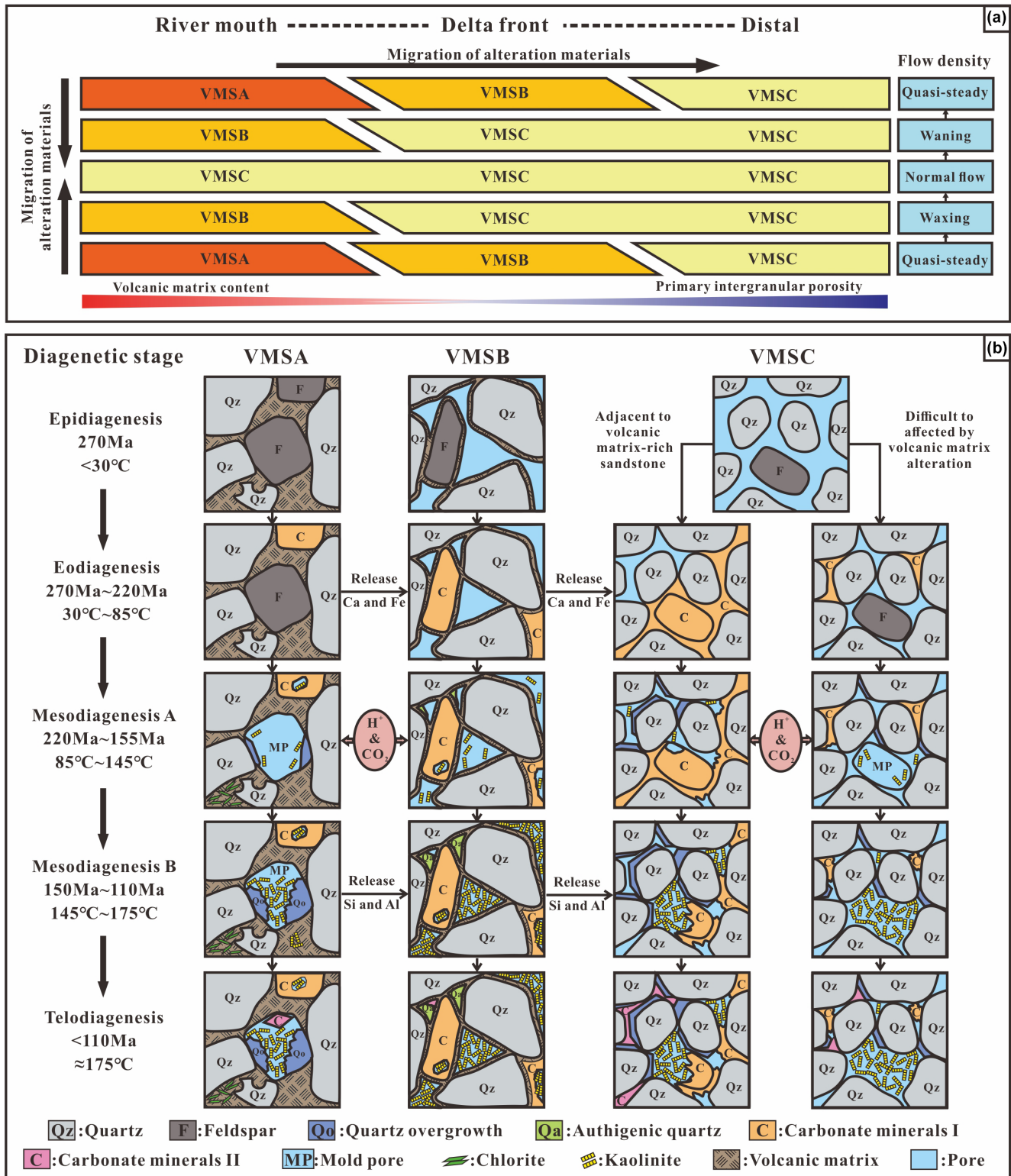


FIGURE 14 (a) The trend of alteration material migration between hyperpycnites and normal sediments. (b) Diagenetic schematic model summarises the diagenetic intensity differences of three types of VMS. There are obvious differences in diagenetic intensity, but with uniform paragenetic sequence.

Telodiagenesis was characterised by the low content of ferroan calcite cements. The late carbonate cements were distributed outside quartz overgrowth and

inside quartz grain fractures, which probably relates to the dissolution and reprecipitation of carbonate cements.

7.4.2 | Diagenetic schematic model

Based on spatial distribution, diagenetic characteristics and alteration material migration, a diagenetic schematic model of P_2S_1 and P_2h_8 is established for the southwestern Ordos Basin (Figure 14).

VMSA was mainly distributed at the river mouth during the peak of eruption period by hyperpycnal flows. Original volcanic matrix tended to be the probable migration point of silica, aluminium and alkaline earth cations during alteration (Altaner, 1990; Slaughter & Earley, 1965). The growth space of authigenic minerals was almost all occupied by the volcanic matrix. Authigenic minerals were mainly presented as in-situ replacement of volcanic matrix, including D-kaolinite, R-kaolinite, chlorite, anatase, etc. (Fisher & Schmincke, 1984). Only a small fraction of these reaction products could precipitate out into the extremely limited mould pores, while the majority were transported to VMSB or VMSC (Altaner, 1990; White et al., 2010). Overall, the main diagenetic characteristics of VMSA can be summarised as follows: extensive alteration of volcanic matrix; strong material transfer to the surroundings; and authigenic mineral precipitation in limited mould pores.

VMSB was often spatially contiguous with VMSA. The reduction of intergranular volcanic matrix content accommodated authigenic mineral growth space. Interior alteration and exterior input from adjacent layers provided sufficient material basis for authigenic mineral precipitation, which in turn led to extensive development of various cements. The intergranular pores were almost completely occupied by authigenic kaolinite and polycrystalline authigenic quartz. Overall, the main diagenetic characteristics of VMSB can be summarised as: a combination of internal and external material sources and the intergranular mixed filling of volcanic matrix and authigenic minerals.

VMSC was often spatially contiguous with VMSB. Volcanic alteration products of VMSA and VMSB would be continuously transported into VMSC. As the distance (including vertical and horizontal direction) from VMSA increased, the content of authigenic minerals gradually declined (Longman et al., 2021). In VMSC, the ion migration sequence of volcanogenic materials during diagenesis determined the precipitation sequence of authigenic minerals, and the ions migration intensity in volcanogenic materials and the distance from VMS determined the authigenic mineral content (Sætre et al., 2018). Overall, the main diagenetic characteristics of VMSC can be summarised as: external material sources and widely developed authigenic minerals.

7.5 | Wider implications

The results of this study have wider implications in the following respects: (1) In terms of regional significance, we propose a multi-volcanic-material source and the possible tectonothermal events in the NQOB during the Permian. A subsequent study on the characteristics of volcanic magmatism in the NQOB could be used to retrace the tectono-magmatic evolutionary history of the orogenic belt under the geotectonic state. (2) This work reveals that the concentrated distribution of volcanogenic materials by long-distance transport were mainly a result of hyperpycnal flows shortly after catastrophic eruption events. This observation fits with previous theoretical work of volcanism-triggered hyperpycnal flows (Dadson et al., 2004; Mulder et al., 2003; Ponciano & Della-Fàvera, 2009). Similar depositional processes can occur in other modern and ancient fluvio-deltaic system within volcanically active mountain belts. (3) Microcrystalline and highly reactive volcanic matrix with great surface area have been altered into stubby quartz cryptocrystal aggregates, indicating that intensive element migration can occur during the burial process. The formation of authigenic minerals related to element migration has a significant influence on sandstone pore spaces. Therefore, the diagenetic schematic model proposed in this study has reference value for the prediction of favourable reservoirs in tuffaceous sandstones.

8 | CONCLUSIONS

Two sets of VMS were developed at the bottom of Permian P_2S_1 and P_2h_8 in the Longdong Region, southwestern Ordos Basin. In this study, adequate applications of petrological, mineralogical and geochemical analytical techniques make it possible to decipher provenance, depositional and diagenetic information contained in the deposits. The following conclusions are obtained:

1. VMS show a greyish white colour, and grain size was generally above medium. They occur mainly as channelised sandstones at the delta plain or river mouth. Volcanogenic material content gradually decreases from southwest to northeast, consistent with paleocurrent direction.
2. The detrital composition of VMS is relatively uniform. The most striking aspect is the presence of abundant quartz and the lower feldspar content. During the subsequent diagenesis, alteration of volcanogenic materials contributes to precipitation of different authigenic minerals, including siliceous, carbonate and clay mineral phases.

3. Detrital zircons used to record the age and duration of P_{2S_1} and P_{2H_8} in the NQOB were discovered in the Permian and Triassic deposits in southern Ordos Basin. Combined with the tectonic setting, geochemical indicators and mapped distribution of volcanogenic material content in the study and adjacent area, we proposed that volcanogenic materials did not derive from the YYOB in the northern basin as previously thought, but from volcanism near the NQOB in the southwest.
4. According to criterion for hyperpycnites in sedimentary structure and lithofacies associations, hyperpycnal flows in the deltaic settings occurred during the deposition of VMS. Based on integration of the current hyperpycnite facies model, a volcanic matrix-rich hyperpycnite model for P_{2S_1} and P_{2H_8} in the southwestern Ordos Basin was proposed. Volcanic matrix content and sedimentary structure in hyperpycnites accurately predicted the flow variation.
5. The cementation strength of authigenic minerals, however, was closely related to pore structure characteristics and the migration trend of volcanic-matrix alteration materials. The origin of sandstones with high volcanic-matrix content can be summarised as related to: an extensive alteration of volcanic matrix, a strong material transfer to the surroundings, and authigenic mineral precipitation in limited mould pores. The origin of sandstones with low volcanic-matrix content can be related to: an input from external material sources followed by the growing of authigenic minerals within the intergranular pores.

ACKNOWLEDGEMENTS

This work was supported by the National Natural Science Foundation of China (41872102; 41202107). We thank PetroChina Changqing Oilfield Company for permission to use industry data for this research. Thanks for the editor, Dr Craig Magee for valuable comments and suggestions, which helped us to significantly improve the manuscript. We also would like to thank the reviewers, Drs John Millett, Carlos Zavala and Nils Lenhardt for valuable comments and constructive modifications that greatly enhanced the manuscript.

CONFLICT OF INTEREST

We declare that we do not have any conflict of interest in connection with the work submitted.

PEER REVIEW

The peer review history for this article is available at <https://publons.com/publon/10.1111/br.12688>.

DATA AVAILABILITY STATEMENT

The data that supports the findings of this study are available in the supplementary material of this article.

REFERENCES

- Altaner, S. P. (1990). Mineralogy, chemistry, and diagenesis of tuffs in the Sucker Creek Formation (miocene), Eastern Oregon. *Clay and Clay Minerals*, 38(6), 561–572. <https://doi.org/10.1346/ccmn.1990.0380601>
- Anjos, S. M. C., De Ros, L. F., & Silva, C. M. A. (2003). Chlorite authigenesis and porosity preservation in the Upper Cretaceous marine sediments of the Santos Basin, offshore eastern Brazil. In R. H. Worden & S. Morad (Eds.), *Clay Mineral Cements in Sandstones* (pp. 289–316). Blackwell Publishing. <https://doi.org/10.1002/9781444304336.ch13>
- Antibus, J. V., Panter, K. S., Wilch, T. I., Dunbar, N., McIntosh, W., Tripathi, A., Bindeman, I., & Blusztajn, J. (2014). Alteration of volcanoclastic deposits at Minna Bluff: Geochemical insights on mineralizing environment and climate during the Late Miocene in Antarctica. *Geochemistry, Geophysics, Geosystems*, 15(8), 3258–3280. <https://doi.org/10.1002/2014gc005422>
- Bhatia, M. R., & Crook, K. A. (1986). Trace element characteristics of Graywackes and tectonic setting discrimination of sedimentary basins. *Contributions to Mineralogy and Petrology*, 92(2), 181–193. <https://doi.org/10.1007/bf00375292>
- Bhattacharya, J. P., & Mac Eachern, J. A. (2009). Hyperpycnal rivers and prodeltaic shelves in the Cretaceous Seaway of North America. *Journal of Sedimentary Research*, 79(3–4), 184–209. <https://doi.org/10.2110/jsr.2009.026>
- Bodnar, R. J. (1993). Revised equation and table for determining the freezing point depression of $H_2O-NaCl$ solutions. *Geochimica et Cosmochimica Acta*, 57(3), 683–684. [https://doi.org/10.1016/0016-7037\(93\)90378-A](https://doi.org/10.1016/0016-7037(93)90378-A)
- Boggs, S. (2006). *Principles of sedimentology and stratigraphy* (p. 64). Pearson Education.
- Burger, K., Zhou, Y., & Ren, Y. (2002). Petrography and geochemistry of tonsteins from the 4th member of the Upper Triassic Xujiahe Formation in southern Sichuan Province, China. *International Journal of Coal Geology*, 49(1), 1–17. [https://doi.org/10.1016/S0166-5162\(01\)00053-2](https://doi.org/10.1016/S0166-5162(01)00053-2)
- Buurman, P., Jongmans, A. G., & PiPujol, M. D. (1998). Clay illuviation and mechanical clay infiltration — Is there a difference? *Quaternary International*, 51–2, 66–69. [https://doi.org/10.1016/S1040-6182\(98\)90225-7](https://doi.org/10.1016/S1040-6182(98)90225-7)
- Camacho, H., Busby, C. J., & Kneller, B. (2002). A new depositional model for the classical turbidite locality at San Clemente State Beach, California. *AAPG Bulletin*, 86(9), 1543–1560. <https://doi.org/10.1306/61eedcf6-173e-11d7-8645000102c1865d>
- Capo, R. C., Whipkey, C. E., Blachère, J. R., & Chadwick, O. A. (2000). Pedogenic origin of dolomite in a basaltic weathering profile, Kohala Peninsula, Hawaii. *Geology*, 28(3), 271–274. [https://doi.org/10.1130/0091-7613\(2000\)028<0271:POODIA>2.3.CO;2](https://doi.org/10.1130/0091-7613(2000)028<0271:POODIA>2.3.CO;2)
- Carothers, W. W., & Kharaka, Y. K. (1978). Aliphatic acid anions in oil-field waters—implications for origin of natural gas. *AAPG Bulletin*, 62, 2441–2453. <https://doi.org/10.1306/clea5521-16c9-11d7-8645000102c1865d>
- Chen, H., Zhu, X., Gawthorpe, R. L., Wood, L. J., Liu, Q., Li, S., Shi, R., & Li, H. (2022). The interactions of volcanism and clastic sedimentation in rift basins: Insights from the Palaeogene-Neogene Shaleitian uplift and surrounding sub-basins, Bohai Bay Basin, China. *Basin Research*, 00, 1–29. <https://doi.org/10.1111/br.12651>
- Chen, R., Wang, F., Li, Z., Evans, N. J., Chen, H. D., & Wei, X. S. (2021). Late Paleozoic provenance shift in the east-central

- Ordos Basin: Implications for the tectonic evolution of the north China Craton. *Journal of Asian Earth Sciences*, 215(1), 104799. <https://doi.org/10.1016/j.jseaeas.2021.104799>
- Collinson, J. D. (1996). Alluvial sediments. In H. G. Reading (Ed.), *Sedimentary environments: Processes, facies and stratigraphy* (pp. 37–82). Blackwell Publishing.
- Cronin, S. J., Neall, V. E., & Palmer, A. S. (1996). Geological history of the north-eastern ring plain of Ruapehu Volcano, New Zealand. *Quaternary International*, 34–36, 21–28. [https://doi.org/10.1016/1040-6182\(95\)00066-6](https://doi.org/10.1016/1040-6182(95)00066-6)
- Crovisier, J. L., Thomassin, J. H., Juteau, T., Eberhart, J. P., Touray, J. C., & Baillif, P. (1983). Experimental seawater-basaltic glass interaction at 50°C: Study of early developed phases by electron microscopy and X-ray photoelectron spectrometry. *Geochimica et Cosmochimica Acta*, 47(3), 377–387. [https://doi.org/10.1016/0016-7037\(83\)90260-0](https://doi.org/10.1016/0016-7037(83)90260-0)
- Cullers, R. L. (2000). The geochemistry of shales, siltstones and sandstones of Pennsylvanian-Permian Age, Colorado, USA: Implications for provenance and metamorphic studies. *Lithos*, 51, 181–203. [https://doi.org/10.1016/s0024-4937\(99\)00063-8](https://doi.org/10.1016/s0024-4937(99)00063-8)
- Dadson, S. J., Hovius, N., Chen, H., Dade, W. B., Lin, J. C., Hsu, M. L., Lin, C. W., Horng, M. J., Chen, T. C., Milliman, J., & Stark, C. P. (2004). Earthquake-triggered increase in sediment delivery from an active mountain belt. *Geology*, 32(8), 733. <https://doi.org/10.1130/g20639.1>
- Dai, S. F., Ward, C. R., Graham, I. T., French, D., Hower, J. C., Zhao, L., & Wang, X. B. (2017). Altered volcanic ashes in coal and coal-bearing sequences: A review of their nature and significance. *Earth-Science Reviews*, 175, 44–74. <https://doi.org/10.1016/j.earscirev.2017.10.005>
- Dickinson, W. R., & Suczek, C. A. (1979). Plate tectonics and sandstone compositions. *AAPG Bulletin*, 63(12), 2164–2182. <https://doi.org/10.1306/2f9188fb-16ce-11d7-8645000102c1865d>
- Dill, H. G. (2016). Kaolin: Soil, rock and ore from the mineral to the magmatic, sedimentary and metamorphic environments. *Earth-Science Reviews*, 161, 16–129. <https://doi.org/10.1016/j.earscirev.2016.07.003>
- Dong, Y. P., & Santosh, M. (2016). Tectonic architecture and multiple orogeny of the Qinling Orogenic Belt, Central China. *Gondwana Research*, 29(1), 1–40. <https://doi.org/10.1016/j.gr.2015.06.009>
- Dong, Y. P., Zhang, G. W., Hauzenberger, C., Neubauer, F., Yang, Z., & Liu, X. M. (2011). Palaeozoic tectonics and evolutionary history of the Qinling Orogen: Evidence from geochemistry and geochronology of ophiolite and related volcanic rocks. *Lithos*, 122(1–2), 39–56. <https://doi.org/10.1016/j.lithos.2010.11.011>
- Ebbinghaus, A., Hartley, A. J., Jolley, D. W., Hole, M., & Millett, J. (2014). Lava-sediment interaction and drainage-system development in a large igneous province: Columbia River Flood Basalt Province, Washington State, U.S.A. *Journal of Sedimentary Research*, 84(11), 1041–1063. <https://doi.org/10.2110/jsr.2014.85>
- Fan, A. P., Yang, R. C., Lenhardt, N., Wang, M., Han, Z. Z., Li, J. B., Li, Y. J., & Zhao, Z. J. (2019). Cementation and porosity evolution of tight sandstone reservoirs in the Permian Sulige gas field, Ordos Basin (Central China). *Marine and Petroleum Geology*, 103, 276–293. <https://doi.org/10.1016/j.marpetgeo.2019.02.010>
- Fisher, R. V., & Schmincke, H. U. (1984). *Pyroclastic rocks* (Vol. 312–345). Springer, Berlin. https://doi.org/10.1007/978-3-642-74864-6_12
- Floyd, P. A., & Leveridge, B. E. (1987). Tectonic environment of the Devonian Gramscatho basin, South Cornwall: Framework mode and geochemical evidence from turbiditic sandstones. *Journal of the Geological Society*, 144(4), 531–542. <https://doi.org/10.1144/gsjgs.144.4.0531>
- Folk, R. L. (1974). *Petrology of sedimentary rocks* (p. 184). Hemphill Publishing.
- Franks, S., & Forester, R. (1984). Relationships among secondary porosity, pore-fluid chemistry and carbon dioxide, Texas Gulf Coast. In D. A. McDonald & R. C. Surdam (Eds.), *Clastic diagenesis* (Vol. 37, pp. 63–80). AAPG Memoir, Tulsa. <https://doi.org/10.1306/m37435c4>
- He, J. C., Zhu, X. M., Liu, M. R., Ye, L., & Xue, M. G. (2017). Parent rock types and tectonic setting of the Permian Shanxi and Shihezi Formations in Longdong area, Ordos Basin. *Journal of Palaeogeography*, 12(2), 285–298. <https://doi.org/10.7605/gdxb.2017.02.022>
- Hesse, R., & Schacht, U. (2011). Early diagenesis of deep-sea sediments. *Developments in Sedimentology*, 63, 557–713. <https://doi.org/10.1016/b978-0-444-53000-4.00009-3>
- Hillier, S., Wilson, M. J., & Merriman, R. J. (2006). Clay mineralogy of the Old Red Sandstone and Devonian sedimentary rocks of Wales, Scotland and England. *Clay Minerals*, 41(1), 433–471. <https://doi.org/10.1180/0009855064110203>
- Hong, H. L., Algeo, T. J., Fang, Q., Zhao, L. L., Ji, K. P., Yin, K., Wang, C. W., & Cheng, S. (2019). Facies dependence of the mineralogy and geochemistry of altered volcanic ash beds: An example from Permian-Triassic transition strata in southwestern China. *Earth-Science Reviews*, 190, 58–88. <https://doi.org/10.1016/j.earscirev.2018.12.007>
- Hower, J. C., Ruppert, L. F., & Eble, C. F. (1999). Lanthanide, yttrium, and zirconium anomalies in the fire clay coal bed, Eastern Kentucky. *International Journal of Coal Geology*, 39(1–3), 141–153. [https://doi.org/10.1016/s0166-5162\(98\)00043-3](https://doi.org/10.1016/s0166-5162(98)00043-3)
- Huff, W. D. (2016). K-bentonites: A review. *American Mineralogist*, 101(1), 43–70. <https://doi.org/10.2138/am-2016-5339>
- Jiang, Z. W., Luo, J. L., Liu, X. S., Hu, X. Y., Ma, S. W., Hou, Y. D., Fan, L. Y., & Hu, Y. H. (2020). Provenance and implication of Carboniferous-Permian detrital zircons from the upper Paleozoic, Southern Ordos Basin, China: Evidence from U-Pb geochronology and Hf isotopes. *Minerals*, 10(3), 265. <https://doi.org/10.3390/min10030265>
- Jin, L., Shan, X., Shi, X., Fonnesu, M., Qiao, S., Kandasamy, S., Wang, H., Liu, S., Fang, X., & Zou, X. (2021). Hybrid event beds generated by erosional bulking of modern hyperpycnal flows on the Choshui River delta front, Taiwan Strait. *Sedimentology*, 68, 2500–2522. <https://doi.org/10.1111/sed.12862>
- Kastner, M., & Gieskes, J. M. (1976). Interstitial water profiles and sites of diagenetic reactions, Leg 35, DSDP, bellingshausen abyssal plain. *Earth and Planetary Science Letters*, 33(1), 11–20. [https://doi.org/10.1016/0012-821x\(76\)90152-7](https://doi.org/10.1016/0012-821x(76)90152-7)
- Kiipili, T., Hints, R., Kallaste, T., Verš, E., & Voolma, M. (2017). Immobile and mobile elements during the transition of volcanic ash to bentonite—An example from the early Palaeozoic sedimentary section of the Baltic Basin. *Sedimentary Geology*, 347, 148–159. <https://doi.org/10.1016/j.sedgeo.2016.11.009>
- Kneller, B. C., & Branney, M. J. (1995). Sustained high-density turbidity currents and the deposition of thick massive sands. *Sedimentology*, 42(4), 607–616. <https://doi.org/10.1111/j.1365-3091.1995.tb00395.x>

- Lenhardt, N., Hornung, J., Hinderer, M., Böhnell, H., Torres-Alvarado, I. S., & Trauth, N. (2011). Build-up and depositional dynamics of an arc front volcanoclastic complex: The Miocene Tepoztlán Formation (Transmexican volcanic belt, central Mexico). *Sedimentology*, *58*, 785–823. <https://doi.org/10.1111/j.1365-3091.2010.01203.x>
- Li, K., Guo, A. L., Gao, C. Y., & Li, H. A. (2015). Tentative discussion on the source area of the Late Triassic Liuyehe basin in North Qinling Mountains and its relationship with the Ordos basin: Evidence from LA-ICP-MS U-Pb dating of detrital zircons. *Geological Bulletin of China*, *34*(8), 1426–1437 (in Chinese with English abstract).
- Li, Y.H., Guo, X.J., Liang, Y., & Wang, K. (2018). Sedimentary characteristics and provenance of the Chang 10 interval of Upper Triassic Yanchang Formation in Ordos Basin. *Journal of Palaeogeography*, *20*(5), 787–802 (in Chinese with English abstract). doi:<https://doi.org/10.7605/gdxb.2018.05.055>
- Liang, J. W., Ma, X. J., & Tao, W. X. (2020). Detrital zircon U-Pb ages of Middle-Late Permian sedimentary rocks from the southwestern margin of the North China Craton: Implications for provenance and tectonic evolution. *Gondwana Research*, *88*, 250–267. <https://doi.org/10.1016/j.gr.2020.07.008>
- Liu, J., Xian, B., Tan, X., Zhang, L., Su, M., Wu, Q., Wang, Z., Chen, P., He, Y., Zhang, S., Li, J., Gao, Y., & Yu, Q. (2022). Depositional process and dispersal pattern of a faulted margin hyperpycnal system: The Eocene Dongying depression, Bohai Bay Basin, China. *Marine and Petroleum Geology*, *135*, 105405. <https://doi.org/10.1016/j.marpetgeo.2021.105405>
- Liu, L., Wen, H., Chen, H., Wang, Z., & Xu, W. (2021). Depositional architectures and evolutionary processes of channel systems in lacustrine rift basins: The Eocene Shahejie Formation, Zhanhua Depression, Bohai Bay Basin. *Marine and Petroleum Geology*, *131*, 105155. <https://doi.org/10.1016/j.marpetgeo.2021.105155>
- Longman, J., Gernon, T., Palmer, M., Jones, M., Stokke, E., & Svensen, H. (2021). Marine diagenesis of tephra aided the Palaeocene-Eocene Thermal Maximum Termination. *Earth and Planetary Science Letters*, *571*, 117101. <https://doi.org/10.1016/j.epsl.2021.117101>
- Luo, S.S., Pan, Z.Y., Lv, Q.Q., He, W.L., & Wen, S. (2017). The Upper Paleozoic detrital zircon U-Pb geochronology and its tectonic significance in southwestern Ordos Basin. *Geology in China*, *44*(3), 556–574 (in Chinese with English abstract). <https://doi.org/10.12029/gc20170312>
- Magee, C., Jackson, C. A. L., & Schofield, N. (2013). The influence of normal fault geometry on igneous sill emplacement and morphology. *Geology*, *41*(4), 407–410. <https://doi.org/10.1130/G33824.1>
- Magee, C., Jackson, C. L., & Schofield, N. (2014). Diachronous sub-volcanic intrusion along deep-water margins: Insights from the Irish Rockall Basin. *Basin Research*, *26*(1), 85–105. <https://doi.org/10.1111/bre.12044>
- Manville, V., Németh, K., & Kano, K. (2009). Source to sink: A review of three decades of progress in the understanding of volcanoclastic processes, deposits, and hazards. *Sedimentary Geology*, *220*, 136–161. <https://doi.org/10.1016/j.sedgeo.2009.04.022>
- Miall, A. D. (1985). Architectural-Element Analysis: A new method of facies analysis applied to fluvial deposits. *Earth-Science Reviews*, *22*(4), 261–308. [https://doi.org/10.1016/0012-8252\(85\)90001-7](https://doi.org/10.1016/0012-8252(85)90001-7)
- Millett, J. M., Jerram, D. A., Manton, B., Planke, S., Ablard, P., Wallis, D., Hole, M. J., Brandsen, H., Jolley, D. W., & Dennehy, C. (2021). The Rosebank Field, NE Atlantic: Volcanic characterisation of an inter-lava hydrocarbon discovery. *Basin Research*, *33*, 2883–2913. <https://doi.org/10.1111/bre.12585>
- Mulder, T., Migeon, S., Savoye, B., & Faugères, J. C. (2001). Inversely graded turbidite sequences in the deep Mediterranean: A record of deposits from flood-generated turbidity currents? *Geo-Marine Letters*, *21*(2), 86–93. <https://doi.org/10.1007/s003670100071>
- Mulder, T., & Syvitski, J. P. (1995). Turbidity currents generated at river mouths during exceptional discharges to the world oceans. *Journal of Geology*, *103*(3), 285–299. <https://doi.org/10.1086/629747>
- Mulder, T., Syvitski, J. P. M., Migeon, S., Faugères, J. C., & Savoye, B. (2003). Marine hyperpycnal flows: Initiation, behavior and related deposits. A review. *Marine and Petroleum Geology*, *20*(6), 861–882. <https://doi.org/10.1016/j.marpetgeo.2003.01.003>
- Murray, N. A., McManus, J., Palmer, M. R., Haley, B., & Manners, H. (2018). Diagenesis in tephra-rich sediments from the Lesser Antilles volcanic arc: Pore fluid constraints. *Geochimica et Cosmochimica Acta*, *228*(2), 119–135. <https://doi.org/10.1016/j.gca.2018.02.039>
- Mutti, E., Davoli, G., Tinterri, R., & Zavala, C. (1996). The importance of ancient fluvio-deltaic systems dominated by catastrophic flooding in tectonically active basins. *Memorie Di Scienze Geologiche*, *48*, 233–291.
- Mutti, E., Tinterri, R., Benevelli, G., Biase, D. D., & Cavanna, G. (2003). Deltaic, mixed and turbidite sedimentation of ancient foreland basins. *Marine and Petroleum Geology*, *20*(6), 733–755. <https://doi.org/10.1016/j.marpetgeo.2003.09.001>
- Mutti, E., Tinterri, R., Biase, D. D., Fava, L., Mavilla, N., Angella, S., & Calabrese, L. (2000). Delta-front facies associations of ancient flood-dominated fluvio-deltaic systems. *Revista de la Sociedad Geológica de España*, *13*(2), 165–190.
- Paredes, J. M., Giacosa, R. E., & Heredia, N. (2009). Sedimentary Evolution of Neogene continental deposits (ñirihuau formation) along the ñirihuau river, North Patagonian Andes of Argentina. *Journal of South American Earth Sciences*, *28*, 74–88. <https://doi.org/10.1016/j.jsames.2009.01.002>
- Petter, A. L., & Steel, R. J. (2006). Hyperpycnal flow variability and slope organization on an Eocene shelf margin, central basin, Spitsbergen. *AAPG Bulletin*, *90*(10), 1451–1472. <https://doi.org/10.1306/04240605144>
- Plink-Björklund, P., & Steel, R. J. (2004). Initiation of turbidity currents: Outcrop evidence for Eocene hyperpycnal flow turbidites. *Sedimentary Geology*, *165*(1–2), 29–52. <https://doi.org/10.1016/j.sedgeo.2003.10.013>
- Ponciano, L. C., & Della-Fávera, J. C. (2009). Flood-dominated fluvio-deltaic system: A new depositional model for the Devonian Cabeças Formation, Parnaíba Basin, Piauí, Brazil. *Anais da Academia Brasileira de Ciências*, *81*(4), 769–780. <https://doi.org/10.1590/s0001-37652009000400014>
- Rard, J. A. (1985). Chemistry and thermodynamics of europium and some of its simpler inorganic compounds and aqueous species. *Chemical Reviews*, *85*, 555–582. <https://doi.org/10.1021/cr00070a003>
- Ratschbacher, L., Hacker, B. R., Calvert, A., Webb, L. E., Grimmer, J. C., McWilliams, M. O., Ireland, T., Dong, S. W., & Hu, J. M. (2003). Tectonics of the Qinling (Central China): Tectonostratigraphy,

- geochronology, and deformation history. *Tectonophysics*, 366, 1–53. [https://doi.org/10.1016/s0040-1951\(03\)00053-2](https://doi.org/10.1016/s0040-1951(03)00053-2)
- Reidel, S. P., & Tolan, T. L. (2013). The late Cenozoic evolution of the Columbia River system in the Columbia River Flood Basalt Province: The Columbia River Flood Basalt Province. *Special Paper of the Geological Society of America*, 497(8), 201–230. [https://doi.org/10.1130/2013.2497\(08\)](https://doi.org/10.1130/2013.2497(08))
- Richards, A., Argles, T., Harris, N., Parrish, R., Ahmad, T., Darbyshire, F., & Draganits, E. (2005). Himalayan architecture constrained by isotopic tracers from clastic sediments. *Earth and Planetary Science Letters*, 236, 773–796. <https://doi.org/10.1016/j.epsl.2005.05.034>
- Sætre, C., Hellevang, H., Dennehy, C., Dypvik, H., & Clark, S. (2018). A diagenetic study of intrabasaltic siliciclastics sandstones from the Rosebank Field. *Marine and Petroleum Geology*, 98, 335–355. <https://doi.org/10.1016/j.marpetgeo.2018.08.026>
- Schmidt, V., & McDonald, D. A. (1979). The role of secondary porosity generation in the course of sandstone diagenesis. In P. A. Scholle & P. R. Schluger (Eds.), *Aspects of diagenesis* (Vol. 26, pp. 175–207). SEPM Special Publication, Tulsa.
- Shchepetkina, A., Gingras, M. K., & Pemberton, S. G. (2018). Modern observations of floccule ripples: Petitcodiac River estuary, New Brunswick, Canada. *Sedimentology*, 65(2), 582–596. <https://doi.org/10.1111/sed.12393>
- Shen, Y. L., Guo, Y. H., Li, Z. F., Wei, X. S., Xue, L. X., & Liu, J. B. (2017). Distribution of radioactive elements (U, Th) in the Upper Paleozoic coal-bearing strata of the eastern Ordos Basin. *Journal of Petroleum Science and Engineering*, 157, 1130–1142. <https://doi.org/10.1016/j.petrol.2017.08.032>
- Slaughter, M., & Earley, J. W. (Eds.). (1965). Mineralogy and geological significance of the Mowry bentonites, Wyoming. In *Geological society of America special paper* (pp. 1–96). Geological Society of America.
- Song, L. J., Chen, J. L., Zhang, Y. L., Liu, C. Y., Wu, C. L., & Zhang, X. H. (2010). U-Pb chronological characteristics of Late Triassic sediment in Southwestern Ordos and its tectonic significance. *Acta Geologica Sinica*, 84(3), 370–386 (in Chinese with English abstract).
- Sparks, R. S., Bonnecaze, R. T., Huppert, H. E., Lister, J. R., Hallworth, M. A., Mader, H., & Phillips, J. (1993). Sediment-laden gravity currents with reversing buoyancy. *Earth and Planetary Science Letters*, 114, 243–257. [https://doi.org/10.1016/0012-821x\(93\)90028-8](https://doi.org/10.1016/0012-821x(93)90028-8)
- Spears, D. A. (2012). The origin of tonsteins, an overview, and links with seatearths, fireclays and fragmental clay rocks. *International Journal of Coal Geology*, 94, 22–31. <https://doi.org/10.1016/j.coal.2011.09.008>
- Steel, E., Simms, A. R., Warrick, J., & Yokoyama, Y. (2016). Highstand shelf fans: The role of buoyancy reversal in the deposition of a new type of shelf sand body. *Geological Society of America Bulletin*, 128(11), 1717–1724. <https://doi.org/10.1130/b31438.1>
- Stefansson, A., & Gislason, S. R. (2001). Chemical weathering of basalts, southwest Iceland: Effect of rock crystallinity and secondary minerals on chemical fluxes to the Ocean. *American Journal of Science*, 301(6), 513–556. <https://doi.org/10.2475/ajs.301.6.513>
- Summa, L. L., & Verosub, K. L. (1992). Trace element mobility during early diagenesis of volcanic ash: Applications to stratigraphic correlation. *Quaternary International*, 13, 149–157. [https://doi.org/10.1016/1040-6182\(92\)90022-t](https://doi.org/10.1016/1040-6182(92)90022-t)
- Sumner, E. J., Amy, L. A., & Talling, P. J. (2008). Deposit structure and processes of sand deposition from decelerating sediment suspensions. *Journal of Sedimentary Research*, 78, 529–547. <https://doi.org/10.2110/jsr.2008.062>
- Sun, D., Feng, Q., Liu, Z., & Xia, L. (2017). Detrital zircon U-Pb dating of the Upper Triassic Yanchang Formation in southwestern Ordos Basin and its provenance significance. *Acta Geologica Sinica*, 91(11), 2521–2544 (in Chinese with English abstract).
- Sun, X. P., Xu, X. Y., Chen, J. L., Gao, T., Li, T., Li, X. B., & Li, X. Y. (2013). Geochemical characteristics and chronology of the Jiangligou granitic pluton in west Qinling and their geological significance. *Acta Geologica Sinica*, 87(3), 330–342 (in Chinese with English abstract).
- Tan, C., Ruan, Z., Yu, B.S., Liu, C., & Su, L. (2019). Tectonics-provenance-palaeogeomorphology system evolution of the western margin of Ordos Basin during the Middle-Late Triassic: The evidences from U-Pb detrital zircon geochronology, geochemistry and petrology. *Acta Petrologica Sinica*, 40(6), 660–676 (in Chinese with English abstract). doi:<https://doi.org/10.7623/syxb201906003>
- Ver Straeten, C. A. (2004). K-bentonites, volcanic ash preservation, and implications for early to Middle Devonian volcanism in the Acadian orogen, eastern North America. *Geological Society of America Bulletin*, 116(3), 474. <https://doi.org/10.1130/b25244.1>
- Viroille, M., Brigaud, B., Bourillot, R., Féniès, H., Portier, E., Duteil, T., Nouet, J., Patrier, P., & Beaufort, D. (2018). Detrital clay grain coats in estuarine clastic deposits: Origin and spatial distribution within a modern sedimentary system, the Gironde estuary (south-west France). *Sedimentology*, 66, 859–894. <https://doi.org/10.1111/sed.12520>
- White, J. D. L., & Houghton, B. F. (2006). Primary volcanoclastic rocks. *Geology*, 34, 677–680. <https://doi.org/10.1130/g22346.1>
- White, R. J., Spinelli, G. A., Mozley, P. S., & Dunbar, N. W. (2010). Importance of volcanic glass alteration to sediment stabilization: Offshore Japan. *Sedimentology*, 58(5), 1138–1154. <https://doi.org/10.1111/j.1365-3091.2010.01198.x>
- Wilson, R. D., & Schieber, J. (2014). Hyperpycnites in the Lower Genesee Group of Central New York, USA: Implications for mud transport in epicontinental seas. *Journal of Sedimentary Research*, 84(10), 866–874. <https://doi.org/10.2110/jsr.2014.70>
- Wilson, R. D., & Schieber, J. (2017). Sediment transport processes and lateral facies gradients across a muddy shelf: Examples from the Genesee Formation of Central New York, United States. *AAPG Bulletin*, 101(4), 423–431. <https://doi.org/10.1306/021417dig17093>
- Worden, R. H., & Morad, S. (2003). Clay minerals in sandstones: Controls on formation, distribution. In R. H. Worden & S. Morad (Eds.), *Clay mineral cements in sandstones* (pp. 3–41). Blackwell Publishing.
- Xian, B. Z., Wang, J. H., Gong, C. L., Yin, Y., Chao, C. Z., Liu, J. P., Zhang, G. D., & Yan, Q. (2018). Classification and sedimentary characteristics of lacustrine hyperpycnal channels: Triassic outcrops in the south Ordos Basin, central China. *Sedimentary Geology*, 368, 68–82. <https://doi.org/10.1016/j.sedgeo.2018.03.006>
- Xie, X. (2016). Provenance and sediment dispersal of the Triassic Yanchang Formation, southwest Ordos Basin, China, and its implications. *Sedimentary Geology*, 335, 1–16. <https://doi.org/10.1016/j.sedgeo.2015.12.016>
- Yang, J. H., Wu, F. Y., Shao, J. A., Wilde, S. A., Xie, L. W., & Liu, X. M. (2006). Constraints on the timing of uplift of the Yanshan

- fold and thrust belt, North China. *Earth and Planetary Science Letters*, 246(3–4), 336–352. <https://doi.org/10.1016/j.epsl.2006.04.029>
- Yang, T., Zhang, Y. F., Yang, L., Yi, P. F., He, Y. F., & Wu, T. (2018). Detrital zircon U-Pb age of Mesozoic Donghe Group in South Qinling Mountain and its geological significance. *Acta Petrologica et Mineralogica*, 37, 211–229 (in Chinese with English abstract).
- Zavala, C., & Arcuri, M. (2016). Intrabasinal and extrabasinal turbidites: Origin and distinctive characteristics. *Sedimentary Geology*, 337, 36–54. <https://doi.org/10.1016/j.sedgeo.2016.03.008>
- Zavala, C., Arcuri, M., Meglio, M. D., Diaz, H. G., & Contreras, C. (2011). A genetic facies tract for the analysis of sustained hyperpynal flow deposits. In C. Zavala & R. Slatt (Eds.), *Sediment transfer from shelf to deep water-revisiting the delivery system* (Vol. 61, pp. 31–51). AAPG Studies in Geology, Tulsa.
- Zavala, C., Ponce, J. J., Arcuri, M., Dritanti, D., Freije, H., & Asensio, M. (2006). Ancient lacustrine hyperpynites: A depositional model from a case study in the Rayoso Formation (Cretaceous) of west-central Argentina. *Journal of Sedimentary Research*, 76(1–2), 41–59. <https://doi.org/10.2110/jsr.2006.12>
- Zhang, S. H., Zhao, Y., Song, B., Yang, Z. Y., Hu, J. M., & Wu, H. (2007). Carboniferous granitic plutons from the northern margin of the North China block: Implications for a late Paleozoic active continental margin. *Journal of the Geological Society*, 164, 451–463. <https://doi.org/10.1144/0016-76492005-190>
- Zhao, P., Jahn, B. M., Xu, B., Liao, W., & Wang, Y. Y. (2016). Geochemistry, geochronology and zircon Hf isotopic study of peralkaline-alkaline intrusions along the northern margin of the North China Craton and its tectonic implication for the southeastern Central Asian Orogenic Belt. *Lithos*, 261, 92–108. <https://doi.org/10.1016/j.lithos.2015.12.013>
- Zhu, S. F., Cui, H., Chen, J. H., Luo, G. J., Wang, W. Y., Yang, Y., & Shi, Y. (2021). Sedimentary system and sandstone reservoir petrology of a shallow water delta: Case study of the Shan-1 and He-8 members in the western Ordos Basin. *Acta Sedimentologica Sinica*, 39(1), 126–139. <https://doi.org/10.14027/j.issn.1000-0550.2020.115> (in Chinese with English abstract).
- Zhu, S. F., Jia, Y., Cui, H., Dowey, P. J., Taylor, K. G., Zhu, X. M., & Liang, T. (2019). Alteration and burial dolomitization of fine-grained, intermediate volcanoclastic rocks under saline-alkaline conditions: Bayindulan Sag in the Er'Lian Basin, China. *Marine and Petroleum Geology*, 110, 621–637. <https://doi.org/10.1016/j.marpetgeo.2019.07.045>
- Zhu, S. F., Wang, X. X., Qin, Y., Jia, Y., Zhu, X. M., Zhang, J. T., & Hu, Y. Q. (2017). Occurrence and origin of pore-lining chlorite and its effectiveness on preserving porosity in sandstone of the Middle Yanchang Formation in the Southwest Ordos Basin. *Applied Clay Science*, 148(C), 25–38. <https://doi.org/10.1016/j.clay.2017.08.005>
- Zhu, S. F., Zhu, X. M., Jia, Y., Cui, H., & Wang, W. Y. (2020). Diagenetic alteration, pore-throat network, and reservoir quality of tight gas sandstone reservoirs: A case study of the upper Paleozoic sequence in the northern Tianhuan Depression in the Ordos Basin, China. *AAPG Bulletin*, 104(11), 2297–2324. <https://doi.org/10.1306/08151919058>
- Ziegler, K. (2006). Clay minerals of the Permian Rotliegend Group in the North Sea and adjacent areas. *Clay Minerals*, 41(1), 355–393. <https://doi.org/10.1180/0009855064110200>
- Zielinski, R. A. (1985). Element mobility during alteration of silicic ash to kaolinite—a study of tonstein. *Sedimentology*, 32(4), 567–579. <https://doi.org/10.1111/j.1365-3091.1985.tb00471.x>

How to cite this article: Cui, H., Zhu, S., Tan, M., & Tong, H. (2022). Depositional and diagenetic processes in volcanic matrix-rich sandstones from the Shanxi and Shihezi formations, Ordos Basin, China: Implication for volcano-sedimentary systems. *Basin Research*, 34, 1859–1893. <https://doi.org/10.1111/bre.12688>

APPENDIX A

Chemical composition of tuffaceous interlayer samples from the Longdong Region

Sample	Well	Depth (m)	Member	Element															
				Sc	V	Cr	Sr	Ba	Pb	Rb	Th	U	Ge	Co	Ni	Nb	Hf	TiO ₂	
Trace element and TiO₂				10 ⁻⁶	%														
1	QT2	4733.8	P ₂ h ₈	18.3	91.9	70.4	238	1105	21.7	183	34.9	5.55	1.90	5.24	29.0	29.8	6.68	0.76	
2	QT2	4794.25	P ₂ s ₁	17.9	98.8	62.7	185	962	34.6	211	33.2	5.30	1.68	14.2	34.1	21.5	5.01	0.79	
3	QT2	4795.01	P ₂ s ₁	15.9	102	54.5	163	925	33.7	191	32.8	5.74	1.54	6.76	19.6	22.9	5.86	0.86	
4	QT2	4733.80	P ₂ h ₈	15.2	96.2	64.2	227	993	22.6	175	17.5	4.90	2.08	6.21	29.2	21.8	5.60	0.63	
5	L1	4223.99	P ₂ s ₁	10.8	37.3	24.3	178	461	17.8	96.9	36.8	8.61	2.00	6.64	14.7	35.5	9.18	0.36	
6	L1	4225.54	P ₂ s ₁	14.3	81.5	123	119	492	15.2	80.1	17.0	9.56	2.38	9.71	23.2	19.1	4.74	0.65	
Rare earth elements				La	Ce	Pr	Nd	Sm	Eu	Gd	Tb	Dy	Y	Ho	Er	Tm	Yb	Lu	
				10 ⁻⁶															
1	QT2	4733.8	P ₂ h ₈	108.70	251.40	25.70	104.70	17.90	2.31	15.40	1.86	10.40	50.20	1.90	5.63	0.80	5.27	0.79	
2	QT2	4794.25	P ₂ s ₁	51.40	108.30	10.80	43.70	7.38	1.11	7.04	0.99	5.59	33.50	1.17	3.36	0.46	3.12	0.48	
3	QT2	4795.01	P ₂ s ₁	44.30	94.50	8.83	33.60	5.32	0.84	5.58	0.76	4.64	27.40	0.97	2.71	0.38	2.49	0.37	
4	QT2	4733.80	P ₂ h ₈	120.80	273.90	33.60	126.10	24.70	3.08	21.60	2.35	14.20	71.80	2.34	7.81	1.00	6.73	0.88	
5	L1	4223.99	P ₂ s ₁	84.20	212.60	26.50	99.70	17.80	2.54	14.00	1.49	8.44	29.80	1.23	4.09	0.53	4.36	0.56	
6	L1	4225.54	P ₂ s ₁	59.20	120.80	12.40	41.20	6.40	1.13	7.29	0.87	5.75	25.40	1.01	3.38	0.46	3.70	0.50	
Rare earth elements standardized by the Upper Continental Crust				La	Ce	Pr	Nd	Sm	Eu	Gd	Tb	Dy	Y	Ho	Er	Tm	Yb	Lu	
				v/v															
1	QT2	4733.8	P ₂ h ₈	3.62	3.93	3.62	4.03	3.98	2.63	4.05	2.91	2.97	2.28	2.38	2.45	2.42	2.40	2.47	
2	QT2	4794.25	P ₂ s ₁	1.71	1.69	1.52	1.68	1.64	1.26	1.85	1.55	1.60	1.52	1.46	1.46	1.39	1.42	1.50	
3	QT2	4795.01	P ₂ s ₁	1.48	1.48	1.24	1.29	1.18	0.95	1.47	1.19	1.33	1.25	1.21	1.18	1.15	1.13	1.16	
4	QT2	4733.80	P ₂ h ₈	4.03	4.28	4.73	4.85	5.49	3.50	5.68	3.67	4.06	3.26	2.93	3.40	3.03	3.06	2.75	
5	L1	4223.99	P ₂ s ₁	2.81	3.32	3.73	3.83	3.96	2.89	3.68	2.33	2.41	1.35	1.54	1.78	1.61	1.98	1.75	
6	L1	4225.54	P ₂ s ₁	1.97	1.89	1.75	1.58	1.42	1.28	1.92	1.36	1.64	1.15	1.26	1.47	1.39	1.68	1.56	

APPENDIX B

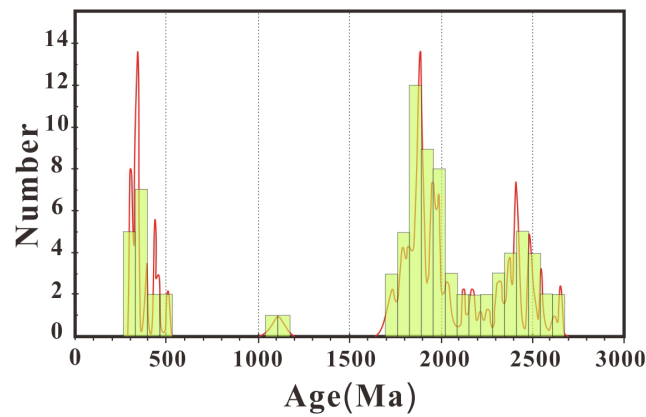
Petrographic features of the main types of fluid inclusion, microthermometric data and salinity data. Salinities are expressed in wt% NaCl eq. and are calculated based on the equation of Bodnar (1993)

Sample	Well	Depth (m)	Member	Lithologies	Size (μm)	The proportion of gas versus liquid phases (%)	Homogenization temperatures (°C)	Salinity (wt% NaCl)
31	CT3	3727.4	P ₂ h ₈	Pebbly sandstone	4×6	≤5	143	14.06
					4×8	≤5	147	14.06
					3×3	≤5	133	14.18
					4×5	≤5	148	14.18
					5×3	≤5	154	14.06
					2×6	≤5	159	14.06
61	Li54	3946.05	P ₂ h ₈	coarse-grained sandstone	2×3	≤5	148	12.94
					6×5	≤5	144	12.94
					2×6	≤5	129	13.07
					3×5	≤5	128	13.07
					3×3	≤5	158	11.05
					7×5	≤5	162	11.05
					1×8	≤5	134	10.91
					3×4	≤5	166	10.91
					3×6	8	177	10.91
					3×5	≤5	124	11.61
					2×4	≤5	137	11.61
					3×8	≤5	139	11.61
65	Li54	3952.28	P ₂ h ₈	Pebbly sandstone	8×11	≤5	133	2.57
					5×6	≤5	133	2.57
					4×5	≤5	137	2.41
					3×4	≤5	141	2.41
					16×6	≤5	161	2.41
190	L3	4065.7	P ₂ s ₁	Pebbly sandstone	5×8	≤5	118	12.42
					2×3	≤5	118	12.42
					10×6	≤5	120	12.55
					2×2	≤5	129	12.55
					2×6	≤5	140	12.55
					1×3	≤5	140	1.91
					2×3	≤5	142	1.91
					10×4	≤5	145	1.74
					2×4	≤5	145	1.74
					7×13	≤5	147	1.91
					5×6	≤5	120	13.2
					5×7	≤5	122	13.2
					5×4	≤5	125	13.2
					6×4	≤5	127	13.07
					7×4	≤5	129	13.07
10×13	≤5	130	13.07					
12×3	≤5	135	13.2					
12×5	≤5	135	13.2					

Sample	Well	Depth (m)	Member	Lithologies	Size (°)	The proportion of gas versus liquid phases (%)	Homogenization temperatures (°C)	Salinity (wt% NaCl)
278	QT2	4735.9	P ₂ h ₈	Pebbly sandstone	2×3	≤5	150	13.69
					3×3	≤5	153	13.69
					2×2	≤5	153	13.82
					2×3	≤5	159	13.82
					2×3	≤5	162	14.06
					2×2	≤5	148	14.18
					2×1	≤5	169	14.18
					2×2	≤5	118	2.07
					4×4	≤5	120	2.07

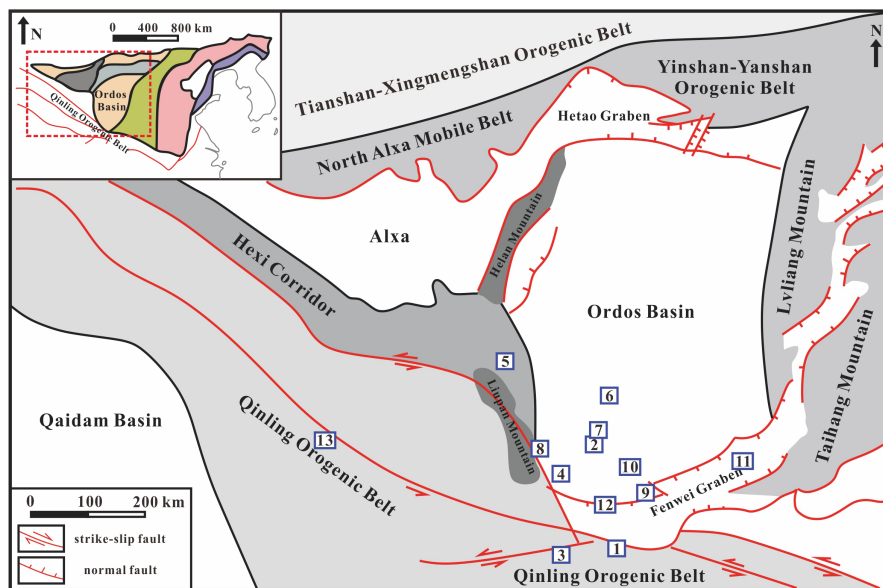
APPENDIX C

Zircon U–Pb dates for VMS in Well QT2 (from He et al., 2017). There are 14 detrital zircon grains with ages between 520–270 Ma, accounting for 16.67% of the total ($n = 84$)



APPENDIX D

Tectonic geological distribution of the Ordos Basin (modified by Tan et al., 2019). The sedimentary topography of the Triassic period in the Longdong Region was relatively steep, and the provenance was mainly from the Qinling Orogenic Belt in the south of Ordos Basin. 1: Liuyehe; 2: Qingyang; 3: Fengxian; 4: Nashiue; 5: Mahuanggou; 6: Huachi; 7: Qingcheng; 8: Pingliang; 9: Jingyang; 10: Binxian; 11: Hancheng; 12: Longfengping and Xifang; 13: Tongren



APPENDIX E

Summary of the Permian detrital zircon ages in the sediments of the Upper Paleozoic P_2h_8 and P_2s_1 in the south of Ordos Basin. Refer to Appendix D for sampling sites

Sampling sites (& number)	Formation	Lithology	Detrital zircon age composition (%) /Ma	Total points	Data sources
Well L2	P_2h_8	Sandstone	271~319 Ma (21%)	$N = 57$	Luo et al. (2017)
Well QT1	P_2s_1	Sandstone	286~309 Ma (13%)	$N = 56$	Luo et al. (2017)
Pingliang-16PL-01	P_2s_1	Sandstone	276.5~355 Ma (9.1%)	$N = 102$	Jiang et al. (2020)
Jingyang-17KZ-01	P_2s_1	Sandstone	285.2~340.5 Ma (5.0%)	$N = 102$	Jiang et al. (2020)
Well CT2-01	P_2s_1	Sandstone	307.9~340.9 Ma (7.8%)	$N = 102$	Jiang et al. (2020)
Bianxian-Luo2-02	P_2s_1	Sandstone	297.7~354.9 Ma (9.1%)	$N = 102$	Jiang et al. (2020)
Hancheng-Yi24-02	P_2s_1	Sandstone	303.2~352.5 Ma (12.7%)	$N = 102$	Jiang et al. (2020)
Bianxian-ChunT1-01	P_2h_8	Sandstone	274.8~354.1 Ma (16.7%)	$N = 102$	Jiang et al. (2020)
Jingyang-17KZ-08	P_2h_8	Sandstone	298.4~340.5 Ma (4.9%)	$N = 102$	Jiang et al. (2020)
Bianxian-Luo2-04	P_2h_8	Sandstone	286.2~352.1 Ma (8.9%)	$N = 101$	Jiang et al. (2020)
Hancheng-16HC-03	P_2h_8	Sandstone	284.8~335.5 Ma (9.9%)	$N = 101$	Jiang et al. (2020)
Hancheng-Yi24-03	P_2h_8	Sandstone	299.7~350.4 Ma (11.8%)	$N = 102$	Jiang et al. (2020)
Well CT2-03	P_2h_8	Sandstone	278.7~344.6 Ma (15.7%)	$N = 102$	Jiang et al. (2020)
Well X1-04	P_2h_8	Sandstone	300.3~344.1 Ma (6.9%)	$N = 102$	Jiang et al. (2020)
Pingliang-16PL-08	P_2h_8	Sandstone	274.5~335.4 Ma (9.0%)	$N = 100$	Jiang et al. (2020)

Sampling sites (& number)	Formation	Lithology	Detrital zircon age composition (%) /Ma	Total points	Data sources
Longfengping-ZR-1	P ₂ h	Quartzarenite	264~350 Ma (16.7%)	N = 72	Liang et al. (2020)
Longfengping-ZR-2	P ₂ h	Quartzarenite	269~342 Ma (13.2%)	N = 91	Liang et al. (2020)
Longfengping-ZR-3	P ₂ h	Quartzarenite	265~339 Ma (21.5%)	N = 93	Liang et al. (2020)
Xifang-ZR-4	P ₂ h	Quartzarenite	256~336 Ma (26.9%)	N = 52	Liang et al. (2020)
Xifang-ZR-5	P ₂ h	Quartzarenite	255~346 Ma (22.2%)	N = 72	Liang et al. (2020)
Xifang-ZR-6	P ₂ h	Quartzarenite	277~346 Ma (16.7%)	N = 72	Liang et al. (2020)
Tongren	Late Middle Permian	Monzonitic granite	260 ± 3~269 ± 3Ma (100%)	N = 17	Sun et al. (2013)

APPENDIX F

Summary of the Permian detrital zircon ages in the Triassic sediments derived from the North Qinling Orogenic Belt. Refer to Appendix D for sampling sites.

Sampling sites (& number)	Formation	Lithology	Detrital zircon age composition (%) /Ma	Total points	Data sources
Liuyehe Basin	Upper Triassic	Quartz sandstone	266~475 Ma (19.5%)	N = 77	Li et al. (2015)
Qingyang-Ning75	Triassic	Sandstone	224~370 Ma (25%)	–	Li et al. (2018)
Qingyang-Xi75	Triassic	Sandstone	272~460 Ma	–	Li et al. (2018)
Fengxian	Triassic	Conglomerate	282~306 Ma (5%)	N = 40	Yang et al. (2018)
Nashuihe-9	Triassic	Sandstone	265~303 Ma (21.3%)	N = 75	Song et al. (2010)
Nashuihe-17	Triassic	Sandstone	263~308 Ma (11.4%)	N = 70	Song et al. (2010)
Mahuanggou	Triassic	Sandstone	230~450 Ma	–	Tan et al. (2019)
Huachi-Li78	Triassic	Sandstone	251.8~298.7 Ma (14.6%)	N = 48	Sun et al. (2017)
Qingcheng-zhuang33	Triassic	Sandstone	290.4~309.9 Ma (13.2%)	N = 53	Sun et al. (2017)
Pingliang-Yan40	Triassic	Sandstone	291.9~317.0 Ma (4.9%)	N = 61	Sun et al. (2017)
Nashuihe-rsh04	Triassic	Sandstone	248.7~300.2 Ma (18.8%)	N = 64	Sun et al. (2017)
Nashuihe	Triassic	Sandstone	252~307 Ma (10%)	N = 90	Xie (2016)